POLITECNICO DI TORINO

Master's Degree in Aerospace Engineering

Master's Degree Thesis

Near-Earth Asteroids Fly-By Trajectory Optimization For Mining Purposes

Supervisors

Prof. Manuela BATTIPEDE

Ing. Luigi MASCOLO

Candidate

Martina BRUNO

October 2024

Abstract

The diminishing availability of Earth's resources has catalyzed the emergence of space mining as a burgeoning industry, with the recent success of missions like OSIRIS-REx underscoring the viability of extracting valuable materials from Near-Earth Asteroids (NEAs). This thesis presents an optimized trajectory framework for asteroid mining missions, focusing on minimizing propellant consumption for reaching these NEAs by means of an electric propulsion system and optimal control theory. The selection process begins with a comprehensive evaluation of potential asteroids, filtering those that are accessible through a Hohmann transfer with a ΔV requirement below a specified threshold. This criterion ensures the chosen asteroids have orbital parameters that closely align with the mission's departure conditions, originating from the Sun-Earth Lagrange Point L2. The proposed mission architecture involves a mother-ship equipped to deploy up to two probes, designed to initiate evaluation operations at asteroids with a Minimum Orbital Intersection Distance (MOID) less than 500 000 km. The strategy for inter-asteroid transfers includes the use of discontinuous impulsive Δv maneuvers at the flyby, not exceeding $1\,\mathrm{km\,s^{-1}}$, to efficiently navigate between target asteroids. The complexity of gravitational interactions among the considered celestial bodies permits nevertheless the utilization of an autonomous switching function based on the bang-bang control, obviating the necessity for a priori specification of thrust arcs to accomplish the intended rendezvous. For precise modeling of heliocentric trajectories and the positions of celestial bodies, this study utilizes the JPL DE440 ephemeris. This high-fidelity model accounts for the gravitational influences of the Sun and the Earth-Moon System.

Acknowledgements

Vorrei ringraziare innanzitutto i miei amici e la mia famiglia, mio padre per avermi sempre spronata e mia madre sostenuta. Ringrazio il mio ragazzo, Edoardo, che mi è sempre stato vicino facendo il tifo per me. Infine, un ringraziamento speciale va ai ragazzi con cui ho condiviso questo progetto, che hanno reso tutto possibile e più leggero, alla professoressa Manuela Battipede, per averci sostenuti, e a Luigi Mascolo, per averci mostrato una disponibilità e dedizione rare.

"Le idee nuove necessitano di spazio"
Paulo Coelho, Manuale del Guerriero della Luce

Table of Contents

List of Tables

List of Figures

Acronyms

ARProbes	Asteroid Reconnaissance Probes
CKP	Classical Keplerian Parameters
CoV	Calculus of Variations
CR3BP	Circular Restricted Three-Body Problem
DC	Differential Corrector
GRASP	Geophysical Reconaissance Asteroid Surface Probe
JPL	Jet Propulsion Laboratory
JPL DE440	Jet Propulsion Laboratory Development Ephemeris
MOID	Minimum Orbital Intersection Distance
MPOCP	Multi-Point Optimal Control Problem
MPBVP	Multi-Point Boundary Value Problem
NASA	National Aeronautics and Space Administration
NBP	N-Body Problem
NEAs	Near-Earth Asteroids
NEOs	Near-Earth Objects
OCP	Optimal Control Problem
OCT	Optimal Control Theory
ODEs	Ordinary Differential Equations
OSIRIS-REx	Origins Spetracl Interpretation Resource Identification and Security - Regolith Explorer
PMP	Pontryagin's Maximum Principle
PmP	Pontryagin's minimum Principle
RNBP	Restricted N-Body Problem
RS	Reference System

STM	State Transition Matrix
TBP	Two-Body Problem
TPBVP	Two Point Boundary Value Problem

Chapter 1

Introduction

In a world where natural resources are growing scarcer by the day, humanity has increasingly focused on the possibility of advancing space exploration as a means to address this challenge. Asteroids are known to contain high quantities of rare metals, such as platinum and gold, in addition to more common elements. Space mining could not only meet the growing demand for these materials but also become a lucrative new frontier, generating significant earnings for companies and governments involved [1].

However, as of today, the techniques and infrastructure needed to conduct such complex missions are still under development. Asteroid mining is a relatively new concept, and only in recent years have companies and agencies made initial attempts. In 2016, the National Aeronautics and Space Administration (NASA) launched the first U.S. mission to collect a sample from the asteroid Bennu, Origins Spetracl Interpretation Resource Identification and Security - Regolith Explorer (OSIRIS-REx) [2], which was successfully returned in 2023. The mission then proceeded to explore the asteroid Apophis without even landing. Additionally, in 2023, NASA initiated the Psyche mission [3], aiming to explore a unique metal-rich asteroid of the same name, which may be the core of an early planet. Asteroid mining could also support scientific research and provide water for future missions, thanks to the presence of ice detected on some of these celestial bodies.

Of particular interest are Near-Earth Asteroids (NEAs), which are easily accessible due to their proximity to Earth. These NEAs can be reached by performing a series of fly-by maneuvers. To ensure the success of such missions, which aim to approach these objects, it is crucial to consider the adopted method and minimize propellant consumption. In the space industry, reducing propellant usage is vital because it translates to the ability to reach greater distances and transport more payload. Consequently, electrical propulsion is the preferred type for these endeavors.

1.1 Near-Earth Asteroids

Near-Earth Objects (NEOs) are celestial bodies with dimensions ranging from a few meters to tens of kilometers and their orbits around the Sun bring them in proximity to Earth's orbit. The majority of these objects are asteroids, so the term NEAs will be used when referring to them. Depending on their size, NEAs can pose a potential hazard to our planet, but they also represent a valuable source of essential resources.

Currently, there are over 34 000 known NEAs, although this number is subject to frequent changes due to their exposure to strong perturbations and the possibility of impacting a planetary surface [4][5]. These objects can be classified based on their dimensions or, as detailed below, by their orbital characteristics (Figure 1.1):

- *Atiras*: their orbits are contained inside the Earth's one, having an aphelion distance smaller than Earth's perihelion distance;
- *Atens*: they cross Earth orbit with a smaller semi-major axis;
- *Apollos*: they cross Earth orbit with a bigger semi-major axis;
- *Armos*: their orbits are external to the Earth's one, having an perihelion distance greater than Earth's aphelion distance;

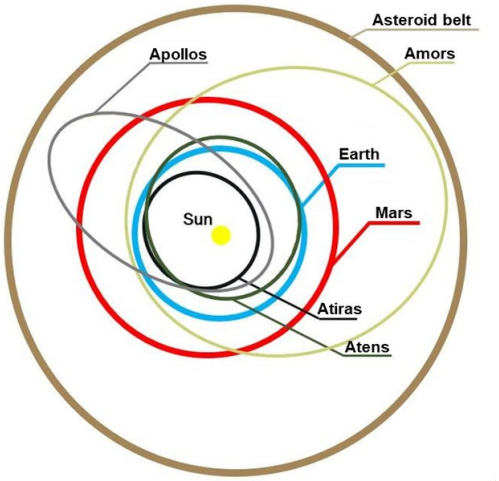

Figure 1.1: NEAs orbital groups [6]

Finally, due to the low surface gravity of NEAs, moving along their surfaces would necessitate only small amounts of energy, making the electrical propulsion system the ideal candidate.

1.2 Low-Thrust Propulsion

When defining a space mission, instead of estimating the total impulse, is better to calculate the total difference in velocity ΔV required for its completion. This quantity also features in the *Tsiolkovsky equation*, formulated in 1903, commonly known as the *rocket equation*. This equation, credited to Russian scientist Konstantin Tsiolkovsky, describes the motion of vehicles that follow the basic principle of a rocket. By expelling part of its mass with high velocity, a rocket can apply acceleration to itself and move due to the conservation of momentum [7]. The equation relates the effective exhaust velocity c, specific impulse I_{sp}, initial total mass (including propellant) m_0, and final total mass (without propellant) m_f to determine the necessary propellant mass for achieving a desired change in velocity:

$$\frac{m_f}{m_0} = e^{-\frac{\Delta V}{c}} \tag{1.1}$$

Since c is defined as the product of the specific impulse I_{sp} and the gravitational acceleration at sea level g_0, and the propellant mass m_p is obtained as the difference between the final mass and the initial one, Equation 1.1 can be rewritten in the form:

$$\frac{m_p}{m_0} = 1 - e^{-\frac{\Delta V}{I_{sp} g_0}} \tag{1.2}$$

The rocket equation plays a crucial role in space exploration, aiding engineers in optimizing propellant usage and achieving mission objectives. By comprehending the relationship between velocity change, propellant mass, and specific impulse, is possible to design more efficient spacecraft for our cosmic endeavors. Specifically, while ΔV represents the cost of reaching the mission goal, I_{sp} defines thruster efficiency: the higher it is, the less propellant is required. This concept is exemplified by the term m_p/m_0, known as the propellant mass fraction, where it becomes evident that increasing specific impulse corresponds to a lower propellant mass. Hence, selecting the appropriate propulsion system is paramount.

Chemical propulsion operates through a chemical reaction in which fuel is oxidized, resulting in the creation of hot gas that expands. Consequently, the thrust generated is so substantial that maneuvers can be approximated as instantaneous impulses. However, the trade-off lies in the relatively low specific impulse values, averaging around 250 s ÷ 350 s, and reaching up to 450 s for liquid bipropellants.

On the other hand, electric propulsion relies on accelerating a mass through an electrostatic or electromagnetic field to generate thrust. Energy for this type of thruster can be supplied via solar panels or batteries and it consumes significantly less propellant than its chemical counterpart. Although the thrust produced is weaker, it compensates with a higher specific impulse, ranging from 200 s up to an

impressive 5 000 s. Despite the longer execution time required for maneuvers (often hours or even days), the superior I_{sp} confirms the advantages of electric propulsion in the realm of trajectory optimization.

1.3 Trajectory Optimization

Orbital trajectory optimization entails designing a spacecraft's path to satisfy specific constraints, such as initial and terminal conditions, while optimizing a relevant quantity (for example minimizing fuel consumption or maximizing mission performance). Additionally, considering the rocket equation, it becomes evident that for every space mission, there exists an optimal value of specific impulse that corresponds to the minimum total mass of the system. This relationship arises because an increase in I_{sp} leads to a decrease in propellant mass, but it also necessitates a higher power source mass for electrical energy generation.

Impulsive trajectories, which use chemical propulsion, can be fully represented with a small number of finite variables. However, low-thrust propulsors, which provide continuous thrust, introduce an infinite-dimensional problem. To address this complexity, it is crucial to define a model that simplifies the problem while maintaining its accuracy. In summary, while impulsive trajectories are straightforward to describe, low-thrust missions require careful modeling to balance complexity and precision.

This problem can be solved numerically implementing iterative procedures that converge within a specified tolerance, integrating multiple sets of differential equations. Such nonlinear optimization methods require an accurate initial guess to achieve convergence, which should be close to the optimal solution or at least a feasible one. Therefore, it's crucial to formulate assumptions about the desired solution's structure. Is evident that solving complex trajectory optimization problems requires a combination of numerical techniques, careful assumptions, and accurate initial conditions [8][9].

This numerical approach can follow two paths: direct and indirect methods.

1.4 Indirect Methods

To solve a problem of infinite dimension, it is possible to apply both direct and indirect methods. Direct methods are easier to implement but require a higher number of variables, which can make them computationally expensive. However, the model's results are more robust and can provide a solution even without fully understanding the problem or its boundary conditions. Nevertheless, the solutions obtained through direct methods may suffer from limited accuracy and require further corrections.

On the other hand, indirect methods require fewer variables and are therefore faster. It is possible to find accurate optimal solutions or, at the very least, obtain additional tools for their search. Typically, for their resolution, an augmented yet simplified problem is created. To ensure convergence, it is crucial to define the necessary conditions based on the specific problem at hand. Consequently, these conditions must be established on a case-by-case basis, necessitating a deep understanding of the involved phenomena [10][11][12].

1.5 Mission Definition

With all these elements, it is possible to define the mission presented here.

The mission begins at Lagrange Point L2. The first step involves creating a database of potential asteroids by filtering the Jet Propulsion Laboratory (JPL) one to select NEAs that meet specific conditions, which will be discussed later.

The proposed architecture includes a mothership weighing 550 kg, equipped with two probes, each weighing 25 kg, designed to evaluate the composition of the target asteroids.

The strategy for inter-asteroid transfers involves using discontinuous impulsive ΔV maneuvers during two flybys, with a maximum magnitude of $1\,\mathrm{km\,s^{-1}}$, to efficiently navigate between target asteroids. Despite the complex gravitational interactions among the celestial bodies considered, an autonomous switching function based on bang-bang control can be employed. This approach eliminates the need for a priori specification of thrust arcs to achieve the desired rendezvous. For precise modeling of heliocentric trajectories and the positions of celestial bodies, this study relies on the Jet Propulsion Laboratory Development Ephemeris (JPL DE440) ephemeris.

Given the problem's complexity, an heliocentric Two-Body Problem (TBP) is used, where the two bodies are the Sun and the mothership, as the asteroid's gravity field is negligible.

Chapter 2

Dynamic Model

To perform an analysis of the optimization problem, it is essential to define the implemented dynamic model. Dynamic models are simplified representations of real-world problems, retaining their essential properties while discarding non-essential ones, and describe how a system evolves over time [13].

To achieve this, a fundamental understanding of orbital mechanics is necessary in order to derive the equations of motion defining the model.

2.1 Orbital Mechanics

Celestial mechanics involves the study of the motion of natural celestial bodies, such as planets and stars. Orbital mechanics extends this concept to include the motion of artificial bodies, like spacecraft and satellites, influenced by gravity and other forces in the space environment. Its primary focus is on analyzing orbital trajectories and planning orbital maneuvers based on Newton's and Kepler's laws [14][15].

2.1.1 N-Body Problem

In celestial mechanics, the N-Body Problem (NBP) describes the absolute motion of celestial bodies in an inertial Reference System (RS) with respect to fixed stars, meaning so far away that they appear immobile.

Under the assumption of point masses and considering only the gravitational attraction forces between the planets, it is possible to obtain the equations of motion for each mass, denoted as m_i. This results in a system of N vectorial (or $3N$ scalar) coupled second-order differential equations that, unfortunately, can only be solved numerically and not analytically. However, is possible to simplify it by focusing on the relative motion of celestial bodies rather than their absolute one.

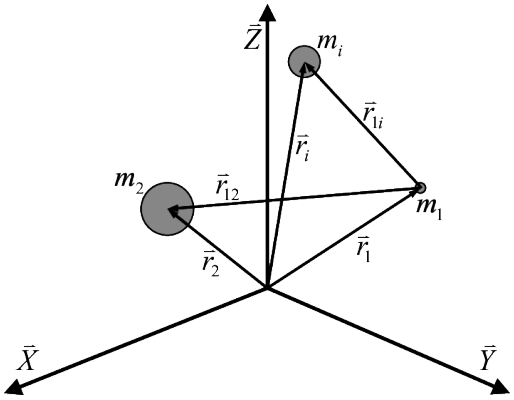

Figure 2.1: N-body problem [16]

For instance, considering their motion relative to the Sun results in the Restricted N-Body Problem (RNBP). When only two bodies are involved, the problem reduces to the TBP, for which an analytical solution exists.

2.1.2 Two-Body Problem

In 1609, Johannes Kepler published three laws regulating the motion of planets in the solar system. These laws are valid for a TBP:

- *Kepler's First Law:* The orbits of the planets are ellipsis, with the Sun at one focus;
- *Kepler's Second Law:* The line joining a planet to the Sun sweeps out equal areas in equal times as the planet travels around the ellipse;
- *Kepler's Third Law:* The ratio of the squares of the periods of revolution for two planets is equal to the ratio of the cubes of their semimajor axes.

The orbits described by Kepler's laws are therefor referred to as *Keplerian* orbits.

Newton's Universal Gravitational Law

Newton's universal law of gravitation states that two bodies are mutually attracted to each other with a force that is directly proportional to the product of their masses and inversely proportional to the square of the distance between them:

$$\vec{F} = -G\frac{mM}{r^2}\frac{\vec{r}}{r} \tag{2.1}$$

In this equation, $G = 6.670 \times 10^{-11}\,\mathrm{N\,m^2\,kg^{-2}}$ represents the universal gravitational constant, while the product GM can be expressed as the gravitational

constant μ, which depends on the major body. By rearranging Equation 2.1, is possible to derive the *equation of motion*:

$$\ddot{\vec{r}} = -\frac{\mu}{r^3}\vec{r} \tag{2.2}$$

Finally, its integration allows to obtain the *trajectory equation* for the TBP:

$$r = \frac{h^2/\mu}{1 + \frac{B}{\mu}cos\nu} \tag{2.3}$$

The term h indicates the angular momentum, B is a constant and ν the *true anomaly*, which is the angle between $\vec{B}$ and $\vec{r}$.

2.1.3 Invariants of the Motion

An invariant of motion is a physical quantity that remains unchanged during such motion. In the context of space trajectories, is possible to identify two key invariants: *mechanical energy* and *angular momentum*.

Conservation of the Mechanical Energy

The equation describing the mechanical energy characteristics of a certain orbit is derived from the equation of motion:

$$E_m = \frac{v^2}{2} - \frac{\mu}{r} = cost \tag{2.4}$$

The first term represents the kinetic energy, while the second represents the potential energy. This quantity remains constant during an orbit, meaning that if one term increases, the other necessarily decreases. Usually, the periapsis of an orbit is characterized by a lower radius and a higher velocity. Therefore, in this position, the kinetic energy is higher while the potential energy is lower. Conversely, the opposite holds true for the apoapsis.

Conservation of the Angular Momentum

From the equation of motion, it is also possible to obtain the angular momentum:

$$|\vec{h}| = rvcos(\varphi)\hat{w} = cost \tag{2.5}$$

Where φ is the flight path angle. This vector is perpendicular to the plane of velocity and remains constant. As a result, the trajectory of the body will remain in a plane, indicating *planar motion*.

2.1.4 Conics

Kepler's first law states that the orbits of the planets are ellipsis, which are a particular type of conic section. Within these geometric figures, is possible to identify a crucial constant, denoted by the symbol e, known as the eccentricity:

$$\frac{r}{d} = cost = e \tag{2.6}$$

The eccentricity indicates how elongated or flattened an ellipse is. It is defined by the ratio between r, which is the distance between the main focus F and a point on the ellipse, and d, the distance between the same point and a reference axis. Depending on its value the orbit will result in a perfect circle, an ellipse, a parabola or an hyperbola. The ellipse is characterized by two foci F and F', a semimajor axis a and a semiminor axis b. The *periapsis* is the point closest to the main focus while the *apoapsis* is the farthest. The radii indicating these two points are determined geometrically:

$$\begin{aligned} r_P &= a(1-e) \\ r_A &= a(1+e) \end{aligned} \tag{2.7}$$

The semilatus rectum p is defined as the point located at a true anomaly of 90°. True anomaly represents the angle indicating the position of the planet with respect to the Sun, starting from the periapsis:

$$p = a(1-e^2) = \frac{h^2}{\mu} \tag{2.8}$$

Therefor, by recalling Equation 2.3 and performing the necessary substitutions, it is possible to derive the conic equation that corresponds to the trajectory equation:

$$r = \frac{a(1-e^2)}{1+ecos\nu} = \frac{p}{1+ecos\nu} \tag{2.9}$$

In Table 2.1, the characteristics of the main conics are reported:

	E_m	e	a
Circle	< 0	$= 0$	> 0
Ellipse	< 0	< 1	> 0
Parabola	$= 0$	$= 1$	∞
Hyperbola	> 0	> 1	> 1

Table 2.1: Conics and their main characteristics

Orbital Period

Having defined the different types of conics, is now possible to determine the time required to travel along one in its entirety. From Kepler's second law:

$$\frac{dA}{dt} = cost \tag{2.10}$$

Is possible to obtain Kepler's third law, which is non other than the orbital period:

$$T = 2\pi\sqrt{\frac{a^3}{\mu}} \tag{2.11}$$

The term a not only represents the semi-major axis, but also the mean distance given by $a = \frac{r_P + r_A}{2}$.

2.1.5 Reference Systems

To study a dynamic problem, it is essential to determine the most suitable RS. The following systems are typically non-inertial but, with certain considerations and conditions, can be treated as inertial. To establish a RS, is necessary to define several fundamental parameters:

- *Origin*: the point from which measurements are taken;
- *Fundamental plane ($x - y$)*: the primary coordinate plane in which the system operates;
- *Principal direction*: the main axis along which motion occurs;
- *Direction of the normal to the plane $x - y$ ($z > 0$)*: the axis perpendicular to the $x - y$ plane, usually pointing upward.

It's important to note that all systems considered here are right-handed, which simplifies determining the last axis, y.

Ecliptic-Heliocentric System

As the name suggests, the heliocentric system places the Sun as its origin and the fundamental plane is the ecliptic, the Earth's orbital plane around the Sun.

The principal axis x is defined by the intersection of the ecliptic and the equatorial plane during the vernal equinox (around March 21). The positive direction of the z axis points toward the north hemisphere, containing the North Star (Polaris). Finally, the y axis is determined by the right-hand rule.

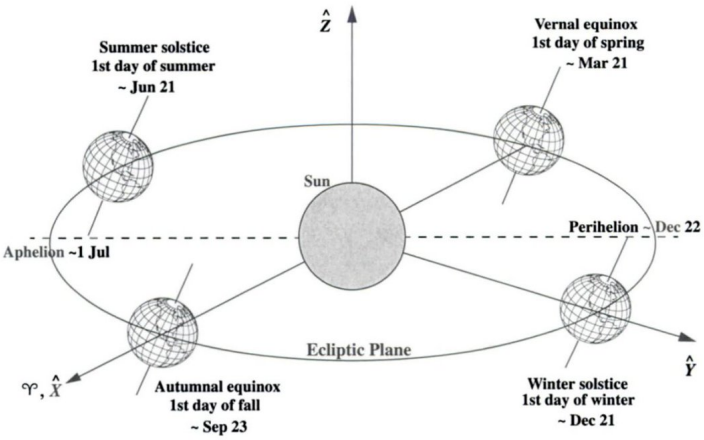

Figure 2.2: Ecliptic-Heliocentric system [17]

Equatorial-Geocentric System

In the geocentric system, the origin is located on Earth and the fundamental plane is represented by the equatorial plane, which is perpendicular to the planet's rotation axis. The principal axis, denoted as x, is determined by the intersection of the equatorial plane with the ecliptic plane. Therefor, this axis corresponds to the one used in the heliocentric system. The positive direction of the z axis is also the same, pointing toward the north hemisphere and Polaris.

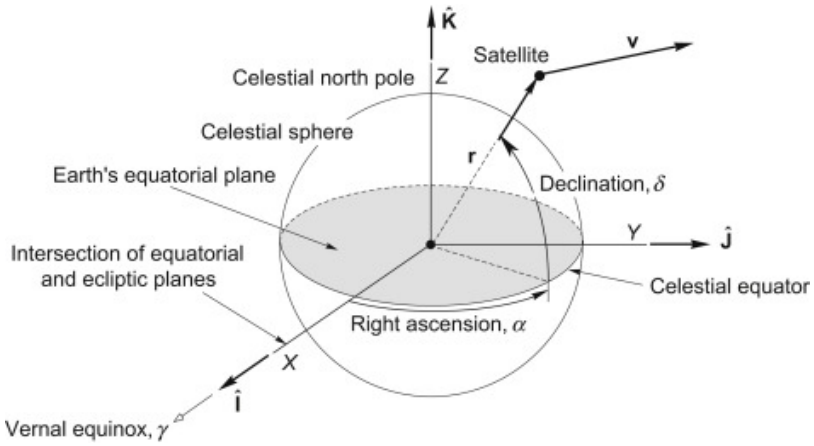

Figure 2.3: Equatorial-Geocentric system [18]

It's important to note that the geocentric system does not rotate with Earth. Figure 2.3 also includes the right ascension α and the declination δ, which are essential angles used in the celestial sphere to locate the position vector of satellites.

Perifocal System

The perifocal system is the most convenient to describe the motion of a smaller body orbiting a larger one.

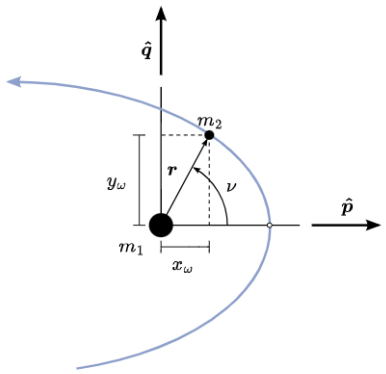

Figure 2.4: Perifocal system [19]

It centers around the focus of the orbit and the fundamental plane is the orbital one. The unit vector $\hat{p}$ points towards the periapsis, while $\hat{q}$ towards the semilatus retum. Unit vector $\hat{w}$ completes the triad and represents the angular momentum vector, being perpendicular to the plane. In summary, the perifocal system simplifies orbital motion by reducing it from three dimensions to two dimensions, making computations easier. It's particularly useful for elliptical orbits, where the coordinate system aligns with the eccentricity vector.

Classical Keplerian Parameters

In orbital mechanics, every existing orbit is uniquely described by six orbital elements, known as the Classical Keplerian Parameters (CKP). Two of these parameters define the size and shape of the ellipse, two more determine the orientation of the orbital plane and the remaining two specify the position of the orbiting body.

Some of these elements have been previously discussed, but here is a comprehensive description:

- Semi-major axis (α): this parameter represents half the distance between the apoapsis (farthest point from the central body) and the periapsis (closest point to the central body). It effectively indicates the size of the elliptical orbit;
- Eccentricity (e): eccentricity describes the shape of the ellipse. A value of 0 corresponds to a perfect circle, while higher values indicate elongation. For instance, highly eccentric orbits resemble stretched ellipses;

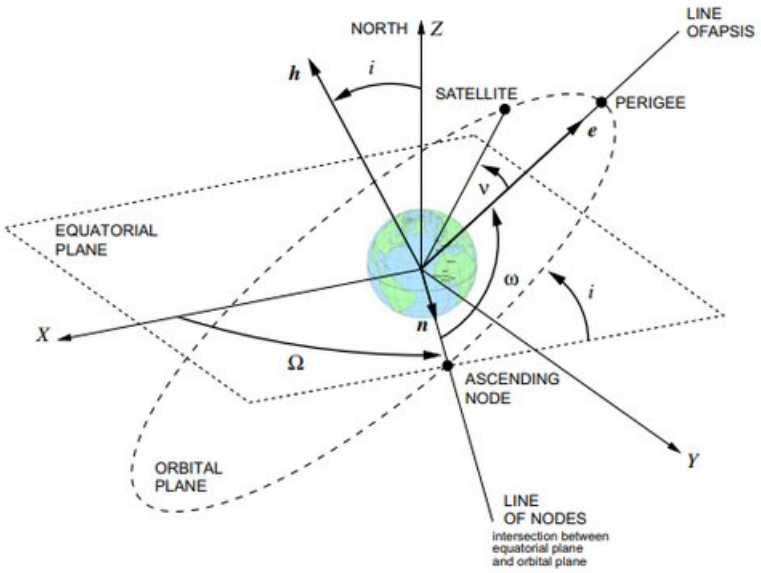

Figure 2.5: Classical Keplerian Parameters [20]

- Longitude of the ascending node (Ω): this element orients the node line $\hat{n}$, which represents the intersection of the orbital plane with the equatorial plane. It is the imaginary line where the orbit transitions from the positive semi-axis to the negative. The point where the orbit crosses the equatorial plane from south to north is called the ascending node;

- Inclination (i): inclination indicates the tilt of the orbit relative to the Z axis. If $i = 0$, the orbit lies in the equatorial plane. A value of 90° corresponds to a polar orbit (where the orbit passes over the poles), while $0° < i < 180°$ covers all other inclinations;

- Argument of periapsis (ω): the argument of periapsis specifies the angular position of the periapsis relative to the node line;

- True anomaly (ν): the true anomaly represents the angular position of the orbiting body from the periapsis. It provides information about the current position along the orbit.

Changing Coordinates

When dealing with different reference frames, it's essential to understand how to switch between them. This operation is known as a *change of basis*, and it involves applying a rotation matrix to transition from one reference frame to another.

Let's focus on transitioning from a perifocal RS ($\hat{p}$, $\hat{q}$, $\hat{w}$) to the geocentric frame ($\hat{I}$, $\hat{J}$, $\hat{K}$) by applying three rotations successively. Euler angles provide a convenient way to express these rotations, making the change of basis more manageable for various orbital problems:

- Rotation of Ω around $\hat{K}$:

$$L_1^T = \begin{bmatrix} \hat{I}\hat{n} & \hat{J}\hat{n} & 0 \\ \hat{I}\hat{m} & \hat{J}\hat{m} & 0 \\ 0 & 0 & 1 \end{bmatrix} = \begin{bmatrix} cos(\Omega) & sin(\Omega) & 0 \\ -sin(\Omega) & cos(\Omega) & 0 \\ 0 & 0 & 1 \end{bmatrix} \tag{2.12}$$

- Rotation of i around $\hat{n}$:

$$L_2^T = \begin{bmatrix} 1 & 0 & 0 \\ 0 & \hat{m}\hat{i} & \hat{K}\hat{m} \\ 0 & \hat{m}\hat{w} & \hat{K}\hat{m} \end{bmatrix} = \begin{bmatrix} 1 & 0 & 0 \\ 0 & cos(i) & sin(i) \\ 0 & -sin(i) & cos(i) \end{bmatrix} \tag{2.13}$$

- Rotation of ω around $\hat{w}$:

$$L_3^T = \begin{bmatrix} \hat{p}\hat{n} & \hat{p}\hat{i} & 0 \\ \hat{q}\hat{n} & \hat{q}\hat{i} & 0 \\ 0 & 0 & 1 \end{bmatrix} = \begin{bmatrix} cos(\omega) & sin(\omega) & 0 \\ -sin(\omega) & cos(\omega) & 0 \\ 0 & 0 & 1 \end{bmatrix} \tag{2.14}$$

As a consequence, the rotation from $\hat{I}$, $\hat{J}$, $\hat{K}$ to $\hat{p}$, $\hat{q}$, $\hat{w}$ is:

$$\vec{r}_{pqw} = L_3^T L_2^T L_1^T \vec{r}_{IJK} = L^T \vec{r}_{IJK} \tag{2.15}$$

Since rotation matrices are orthogonal, their inverse is equal to their transpose. Therefor, to switch from $\hat{p}$, $\hat{q}$, $\hat{w}$ to $\hat{I}$, $\hat{J}$, $\hat{K}$, it is sufficient to remember this characteristic:

$$\vec{r}_{IJK} = L_1 L_2 L_3 \vec{r}_{pqw} = L\vec{r}_{pqw} \tag{2.16}$$

In other words, when dealing with orthogonal rotation matrices, the inverse operation is simply achieved by transposing the matrix. This property simplifies the process of changing coordinate systems and ensures consistency in the transformation. Understanding these fundamental concepts is essential for working with different reference frames in celestial mechanics.

2.1.6 JPL DE440

When facing a spacecraft navigation problem, it is crucial to gather as much information as possible about every celestial body involved in the mission. The JPL has developed a series of mathematical models that represent the positions, velocities, and accelerations of major Solar System bodies [21]. Among these models, the JPL DE440 stands out for its precision. Although there is also a less accurate model called JPL DE441, it covers a much longer period. However, since the mission described in this thesis does not require such extended time coverage, the more precise JPL DE440 model is the preferred choice [22].

2.1.7 Characteristic Velocities

Before delving into the concept of orbital maneuvers, it is essential to define three critical velocities known as characteristic velocities.

Circular Velocity

Circular velocity refers to the spacecraft's velocity along a circular orbit. Its value can be obtained by recalling the energy equation:

$$Eg = \frac{v_c^2}{2} - \frac{\mu}{r} = -\frac{\mu}{2a} \tag{2.17}$$

Taking into account that, in a circular orbit, $r = a$:

$$\frac{v_c^2}{2} = \frac{\mu}{a} - \frac{\mu}{2a} = \frac{\mu}{2r} \tag{2.18}$$

As a result:

$$v_c = \sqrt{\frac{\mu}{r}} \tag{2.19}$$

It's immediately evident that an increasing radius corresponds to a decreasing circular velocity.

Escape Velocity

Escape velocity is the speed that a spacecraft must reach to break free from a planet's gravitational pull. In other words, it's the velocity needed for a secondary body to move infinitely far away from the main body with zero velocity, denoted as $v_\infty = 0$. As seen for the circular velocity, it is possible to obtain its value using the energy equation:

$$Eg = \frac{v_E^2}{2} - \frac{\mu}{r_{BO}} = \frac{0}{2} - \frac{\mu}{r_\infty} = -\frac{\mu}{2a} \tag{2.20}$$

The burnout point corresponds to the position where the impulse is applied. On the left side of Equation 2.20, the energy is associated with the spacecraft's initial orbit, while on the right side, it relates to the infinite distance the spacecraft aims to achieve. Consequently, it results that $a \to \infty$, indicating that the transfer trajectory is parabolic. Considering this:

$$\frac{v_E^2}{2} - \frac{\mu}{r_{BO}} = 0 \tag{2.21}$$

Therefor:

$$v_E = \sqrt{2}\sqrt{\frac{\mu}{r_\infty}} = \sqrt{2}v_c \tag{2.22}$$

It turns out that the escape velocity is equal to the circular velocity multiplied by a factor of $\sqrt{2}$.

Hyperbolic Excess Velocity

Differently from escape velocity, the hyperbolic excess velocity is the speed that a spacecraft needs to achieve in order to move infinitely far away from the main body, escaping its sphere of influence, while maintaining a residual velocity different from zero, meaning $v_\infty \neq 0$. Considering the energy equation one more time:

$$Eg = \frac{v_{BO}^2}{2} - \frac{\mu}{r_{BO}} = \frac{v_\infty^2}{2} - \frac{\mu}{r_\infty} = -\frac{\mu}{2a} \tag{2.23}$$

The term μ/r_∞ is null, therefor:

$$v_\infty = \sqrt{-\frac{\mu}{a}} \tag{2.24}$$

Consequently, given that v_∞ must be positive, the semi-major axis must be negative, indicating a hyperbolic transfer.

2.1.8 Orbital Maneuvers

An orbital maneuver involves applying an impulsive thrust to alter the spacecraft's velocity (ΔV). These maneuvers serve two main purposes: compensating for perturbations (such as gravitational effects) and modifying the orbit's characteristics. Here, a concise definition is provided, categorizing the different types of maneuvers based on the number of impulses required:

- One-Impulse Maneuvers
  - Periapsis/Apoapsis Adjustment: it involves changing the altitude of the spacecraft's orbit by applying thrust at either the periapsis or apoapsis;
  - Abscissa Rotation: by applying thrust at one of the two points where the old and new ellipses intersect, the spacecraft can change its line of apsides, which is the imaginary line connecting the periapsis and apoapsis;
  - Change of Plane: this maneuver involves altering the inclination of the spacecraft's orbit by applying thrust at either the Equator or the apoapsis, which are the most convenient points for executing this maneuver. By doing so, the spacecraft can transition from its current orbital plane to a different one;
  - Combined Maneuver: a combination of the above maneuvers, often used for complex orbital adjustments.
- Two-Impulse Maneuvers
  - Orbit Phasing: used to synchronize the orbits of two spacecraft. The first impulse adjusts the period, and the second aligns the phases;
  - Transfer: a transfer between two circular orbit. The first impulse raises (or lowers) the spacecraft to a higher (or lower) orbit and the second circularizes it, ensuring it becomes a stable circular path;
  - Hohmann Transfer: a particular transfer that minimize the ΔV;
  - Hohmann Transfer (out of plane): similar to the standard Hohmann transfer but performed in a different orbital plane.
- Three-Impulse Maneuvers
  - Bi-elliptic Transfer: a more efficient but complex transfer between two circular orbits. The spacecraft first raises its orbit significantly, then performs a second burn to lower it into the target orbit;
  - Bi-parabolic Transfer: an even more efficient transfer, similar to the bi-elliptic but using parabolic orbits. It's important to note that achieving a true parabolic orbit (where $r = \infty$) is practically impossible due to real-world constraints. The concept serves as a theoretical model rather than a practical maneuver;
  - Change of Plane: achieves a change in inclination by applying thrust at three different points in the orbit.

Each mission may employ a combination of these maneuvers to optimize fuel usage and achieve mission objectives. A prime example of this are interplanetary missions, which will be discussed in a subsequent paragraph. For the purpose of this thesis, a more detailed explanation of Hohmann transfers is also necessary.

Hohmann Transfer

A transfer between circular orbits allows a spacecraft to transition from an initial orbit with a radius of a_1 to a final orbit with a radius of a_2. To achieve this, under the hypothesis that $a_2 > a_1$, the spacecraft receives a first impulse to increase its altitude. It then follows an elliptical transfer orbit until it reaches the final one. Once there, the spacecraft receives a second impulse to decrease its altitude and circularize the final orbit. As a result, the transfer orbit takes the form of an ellipse that intersects both the initial and final orbits.

A Hohmann transfer, as described by Walter Hohmann in his 1925 book *The Attainability of Heavenly Bodies* [23], is a specific type of orbital maneuver that minimizes the required ΔV. It achieves this by applying the first impulse at the periapsis of the elliptical transfer orbit and the second impulse at the apoapsis. As depicted in Figure 2.6, the change in velocity aligns with the spacecraft's velocity vector.

The energy of the transfer orbit is:

$$Eg_H = \frac{v_1^2}{2} - \frac{\mu}{a_1} = \frac{v_2^2}{2} - \frac{\mu}{a_2} = -\frac{\mu}{2a_H} = -\frac{\mu}{r_1 + r_2} \tag{2.25}$$

Knowing the values of the semi-major axis, is easy to obtain the two velocities:

$$\begin{aligned} v_1^2 &= 2\mu\left(\frac{1}{r_1} - \frac{1}{r_1 + r_2}\right) = v_{c1}^2\left(\frac{2r_2}{r_1 + r_2}\right) \rightarrow v_1 > v_{c1} \\ v_2^2 &= 2\mu\left(\frac{1}{r_2} - \frac{1}{r_1 + r_2}\right) = v_{c2}^2\left(\frac{2r_1}{r_1 + r_2}\right) \rightarrow v_2 < v_{c2} \end{aligned} \tag{2.26}$$

Therefor:

$$\begin{aligned} \Delta V_1 &= v_1 - v_{c1} \\ \Delta V_2 &= v_{c2} - v_2 \end{aligned} \tag{2.27}$$

Consequently, is possible to obtain both the total ΔV_H spent and the transfer period:

$$\Delta V_H = \Delta V_1 + \Delta V_2 \tag{2.28}$$

$$T_H = \frac{\tau_H}{2} = \pi\sqrt{\frac{a_H^3}{\mu}} \tag{2.29}$$

To determine the transfer period, it is sufficient to halve the total time spent traveling along the ellipse.

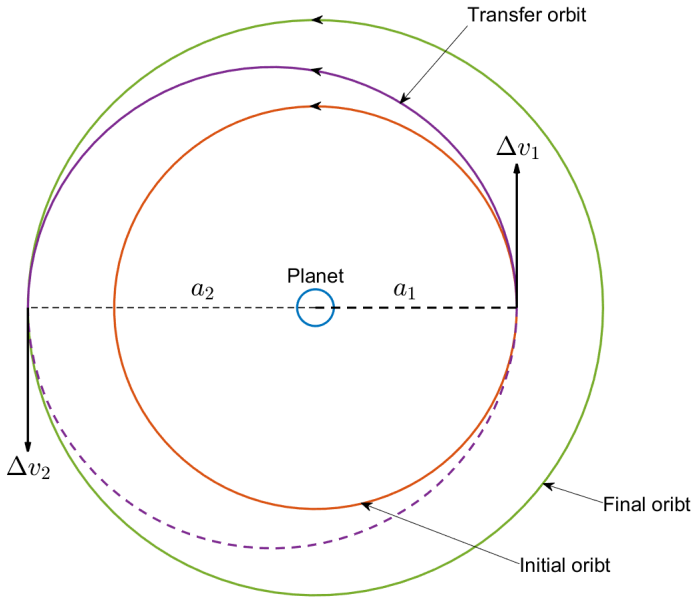

Figure 2.6: Hohmann transfer [24]

2.1.9 Interplanetary Missions

An interplanetary transfer is a maneuver conducted to reach a different planet from the starting one. It is a crucial concept that enables deep-space exploration and must account for all the perturbations that could affect the spacecraft. Interplanetary transfers operate based on the method of patched conics, and the mission can be divided into three segments:

- Departure Phase: a maneuver conducted to exit the sphere of influence of the starting planet;
- Heliocentric Phase: typically involves a Hohmann transfer within the sphere of influence of the Sun;
- Arrival Phase: a maneuver conducted to enter the sphere of influence of the destination planet.

The term *sphere of influence* has been mentioned several times and, in the following paragraph, a definitive definition will be provided.

Patched-Conics Method

The patched-conics method is a technique used in celestial mechanics to analyze the motion of a spacecraft as it travels through space, particularly when encountering

multiple celestial bodies. Each celestial body has a region around it where its gravitational pull dominates over other nearby bodies. This region is called the *sphere of influence* and, within, the gravitational force from that body significantly affects the spacecraft's trajectory [15].

Let's consider two planets as celestial bodies: a larger one of mass m_1 and a smaller one of mass m_2. The radius r_2 that characterizes the minor body's sphere of influence is:

$$r_2 = \left(\frac{m_2}{m_1}\right)^{2.5} r_{12} \tag{2.30}$$

This radius is determined by the balance between the gravitational forces from both bodies. Beyond it, the smaller planet's gravitational pull becomes negligible compared to the larger planet. On the other hand, inside this radius, the smaller planet's gravitational effects are significant.

In summary, as a spacecraft travels through space, it encounters various celestial bodies along its path. The patched-conics method simplifies this complex scenario by dividing the spacecraft's trajectory into segments, each corresponding to a specific sphere of influence. As the spacecraft moves from one sphere of influence to another, its motion is analyzed separately for each segment.

Launch Window

When designing an interplanetary mission, minimizing propellant consumption is crucial. The most effective approach to achieve this goal is by implementing a Hohmann transfer during the heliocentric phase. However, for this transfer to be feasible, it is essential to adhere to the correct launch window. A launch window represents a specific time period during which the mission must be initiated to optimize the transfer's duration and minimize propellant usage [25].

To better explain this concept, let's consider an interplanetary transfer between two planets: Earth and Mars. These planets are respectively represented in blue and red in Figure 2.7. The angle γ_1 indicates the angular distance between Earth's and Mars's initial positions, while γ_2 represents the angular distance between Earth's and Mars's final positions. Earth's initial position at time t_1 and Mars's final position at time t_2 are known. To determine the remaining unknown positions, is necessary to calculate the angular velocities of the planets. These velocities are defined as the rate of change of angle over an entire orbit, corresponding to their orbital periods:

$$\begin{aligned} n_E &= \frac{2\pi}{T_E} \\ n_M &= \frac{2\pi}{T_M} \end{aligned} \tag{2.31}$$

Since this is a Hohmann transfer, the mean distance a_H, which can be calculated as the average of Earth's and Mars's orbital radii, is known. Therefor:

$$\Delta T_H = \frac{T_H}{2} = \pi \sqrt{\frac{a_H^3}{\mu_S}} \tag{2.32}$$

The spacecraft travels only half of the transfer orbit. Additionally, the Sun's gravitational parameter, denoted as μ_S, is considered for the calculations. With this information, is possible to determine the phases of the planets, which represent the angular distance they have traveled along their orbits during this interval:

$$\begin{aligned} f_E &= n_E \Delta T_H \\ f_M &= n_M \Delta T_H \end{aligned} \tag{2.33}$$

Consequently, the launch window is defined as:

$$\gamma_1 = \Delta\nu_{TO} - f_M \tag{2.34}$$

Where, in the case of a Hohmann transfer:

$$\Delta\nu_{TO} = \Delta\nu_H = \pi \tag{2.35}$$

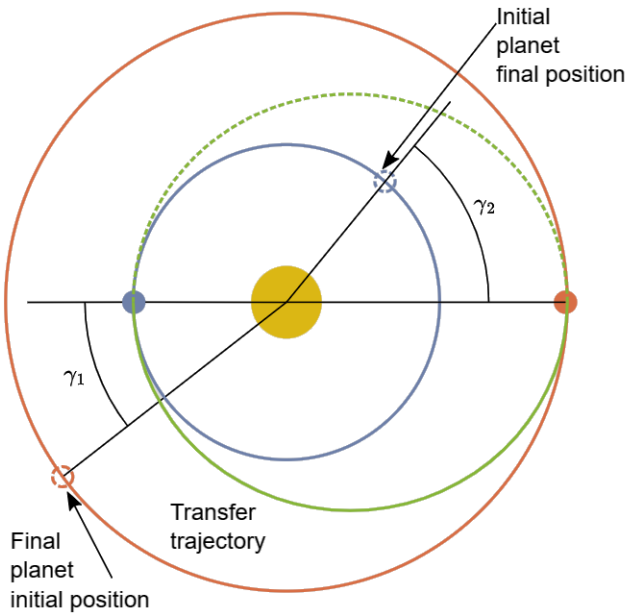

Figure 2.7: Interplanetary phasing [26]

If the launch window is missed, there are two potential strategies to consider:

- *Waiting for a sinodic period T_s*

  The synodic period is the time required for the same launch window to recur. This occurs when the faster celestial body (the inner planet) laps the slower one (the outer planet) twice. In the Earth-Mars case:

$$n_T T_s - n_M T_s = 2\pi \tag{2.36}$$

  Therefor:

$$T_s = \frac{2\pi}{n_T - n_M} \tag{2.37}$$

- *Utilizing a different transfer orbit*

  If a different transfer orbit is used, it is necessary to optimize the $\Delta\nu_{TO}$ in order to reduce the losses due to misalignment and gravitational force.

Heliocentric Phase

When designing an interplanetary mission, the initial step involves studying the heliocentric phase to estimate the required v_∞, meaning the hyperbolic excess velocity, and dimension the departure and arrival hyperbolas. Let's denote V as the velocity relative to the Sun and v as the velocity relative to the orbit. The problem constraints include the initial transfer velocity V_1, the final transfer velocity V_2, and the final alignment angle φ_2. While φ_1 is set to zero, indicating no misalignment during departure, φ_2 is nonzero due to the limited launch window: even a slight delay can lead to a less-than-ideal approach to the arrival planet, resulting in misalignment upon arrival.

There are two possibilities for a transfer, depending on whether the target celestial body is an inner or outer planet:

- *Inner Planet*

  Let's consider a hypothetical transfer from Earth to Venus. In this case, the maneuver involves lowering the periapsis, which means that $V_1 < V_T$. As a consequence:

$$\begin{cases} V_2 > V_1 \\ V_2 > V_V \end{cases} \tag{2.38}$$

  Knowing the semi-major axis of the transfer, it is possible to use the energy equation to estimate the required velocities:

$$Eg = \frac{V_1^2}{2} - \frac{\mu_S}{r_T} = \frac{V_2^2}{2} - \frac{\mu_S}{r_V} = -\frac{\mu_S}{2a_H} = -\frac{\mu_S}{r_T + r_V} \begin{cases} V_1 = V_T\sqrt{\frac{2r_V}{r_T+r_V}} < V_T \\ V_2 = V_V\sqrt{\frac{2r_T}{r_T+r_V}} > V_V \end{cases} \tag{2.39}$$

On the other hand, the momentum allows the calculation of φ_2:

$$h = V_1 r_T = V_2 r_V cos(\varphi_2) \rightarrow \varphi_2 = arccos\left(\frac{V_1 r_T}{V_2 r_V}\right) \tag{2.40}$$

- *Outer Planet*

  Let's now consider a hypothetical transfer from Earth to Mars. In this case, the maneuver involves raising the periapsis, which means that $V_1 > V_T$. As a consequence:

$$\begin{cases} V_2 < V_1 \\ V_2 < V_M \end{cases} \tag{2.41}$$

  Knowing the semi-major axis of the transfer, it is possible to use the energy equation to estimate the required velocities:

$$Eg = \frac{V_1^2}{2} - \frac{\mu_S}{r_T} = \frac{V_2^2}{2} - \frac{\mu_S}{r_M} = -\frac{\mu_S}{2a_H} = -\frac{\mu_S}{r_T + r_M} \begin{cases} V_1 = V_T\sqrt{\frac{2r_M}{r_T+r_M}} > V_T \\ V_2 = V_M\sqrt{\frac{2r_T}{r_T+r_M}} < V_M \end{cases} \tag{2.42}$$

  Again, the momentum allows the calculation of φ_2:

$$h = V_1 r_T = V_2 r_M cos(\varphi_2) \rightarrow \varphi_2 = arccos\left(\frac{V_1 r_T}{V_2 r_M}\right) \tag{2.43}$$

Departing Phase

Having obtained the initial transfer velocity, V_1, during the heliocentric phase, it is now possible to evaluate the departure phase. To escape the sphere of influence of the starting planet, a non-null hyperbolic excess velocity is necessary. Consequently, the spacecraft will follow a hyperbolic trajectory. In simpler terms, the spacecraft begins the mission by orbiting the starting planet with a circular velocity. Then, a first Δv_1 maneuver propels it to a starting hyperbolic transfer velocity, v_p, at the periapsis. Finally, the spacecraft exits the sphere of influence with a relative velocity, v_∞, which, when combined with the celestial body's velocity, equals the

known V_1. Therefore, it is possible to use this last data to calculate the initial velocity backward.

The departure phase changes depending if the target celestial body is an inner or outer planet:

- *Inner Planet*

  To reach an inner planet, the spacecraft must exit the sphere of influence of the starting planet, let's suppose Earth, with an optimal hyperbolic excess velocity, denoted as v_∞. This velocity should be parallel to the starting planet's one, V_T, and satisfy the condition $v_\infty = V_1 - V_T$. This maneuver is commonly referred to as a *back-door exit*, being v_∞ opposite to V_T.

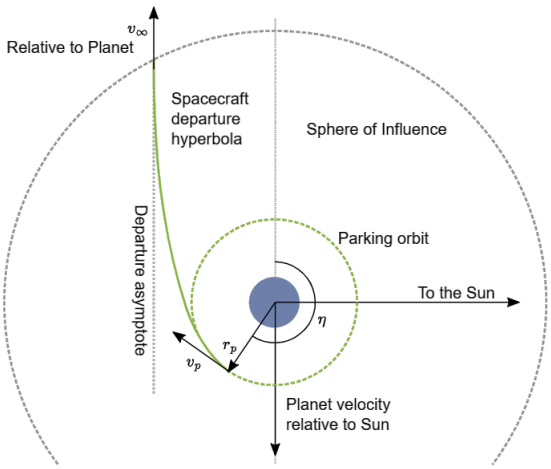

Figure 2.8: Departure from an inner planet [26]

- *Outer Planet*

  To reach an outer planet, the spacecraft's hyperbolic excess velocity v_∞ must be parallel to the planet's velocity V_T and have the same direction. Initially, the spacecraft is in a circular parking orbit with a velocity of $v_c = \sqrt{\frac{\mu_T}{r_c}}$. At periapsis, a propulsion impulse is applied to transition the orbit from circular to hyperbolic, initiating the escape maneuver:

$$v_p = v_c + \Delta v_1 \tag{2.44}$$

  To find the unknown value Δv_1, let's consider the parallel vectors V_1, V_T and v_∞, which satisfy the condition $V_1 = V_T + v_\infty$. By utilizing the energy equation in the context of hyperbolic escape, it is possible to determine the semi-major axis of such a trajectory:

$$Eg = \frac{v_\infty^2}{2} - \frac{\mu_T}{r_\infty} \rightarrow a = -\frac{\mu_T}{v_\infty^2} \tag{2.45}$$

If the energy equation is expressed with respect to the periapsis, it is also possible to determine the periapsis velocity v_p:

$$Eg = \frac{v_p^2}{2} - \frac{\mu_T}{r_c} = \frac{v_\infty^2}{2} \rightarrow v_p = \sqrt{2v_c^2 + v_\infty^2} \tag{2.46}$$

Therefor:

$$\Delta v_1 = v_p - v_c \tag{2.47}$$

In simpler terms, by first solving the heliocentric phase, the velocity V_1 becomes a known quantity. Then, working backwards, is possible to determine the initial impulse required to initiate the mission.

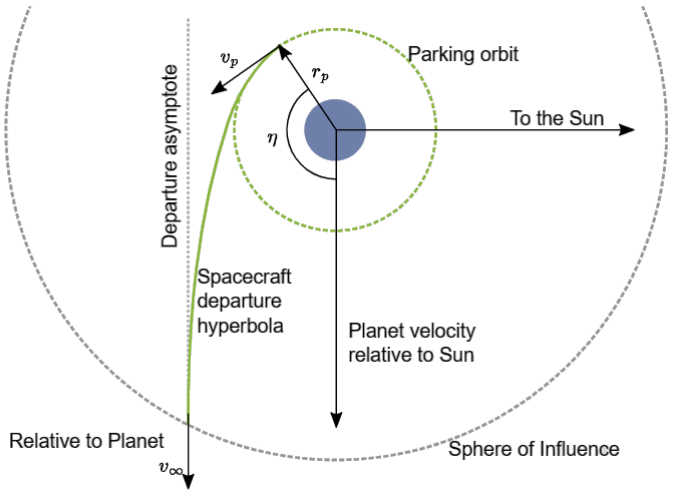

Figure 2.9: Departure from an outer planet [26]

It's worth noting that the transfer could also be parabolic, but in that case, the hyperbolic excess velocity would be zero. Consequently, a second impulse at the asymptotic distance r_∞ would be necessary to achieve the desired velocity V_1. However, opting for a two-impulse maneuver like this would result in higher propellant consumption, making the hyperbolic transfer the preferred choice.

Arrival Phase

In the arrival phase, the spacecraft enters the sphere of influence of the target planet with a hyperbolic excess velocity v_∞. From the heliocentric phase, the values for V_2 and φ_2 are obtained, which will now be used to determine the parameters of the final orbit.

- *Inner Planet*

  When a spacecraft approaches an inner planet, it will follow it, since it is faster. This implies that the spacecraft's velocity, denoted as V_2, is greater than the velocity of the celestial body. The relative velocity of the spacecraft with respect to the planet, in module, is then given by:

  $$v_2 = \sqrt{V_2^2 + V_V^2 - 2V_2V_V cos(\varphi_2)} \tag{2.48}$$

  The energy will be:

  $$Eg = \frac{v_2^2}{2} - \frac{\mu_V}{r_\infty} = -\frac{\mu_V}{2a} \rightarrow a = -\frac{\mu_V}{v_2} \tag{2.49}$$

  From the momentum, a new quantity dm is found:

  $$|\vec{h}| = r_2 v_2 sin\left(\frac{\pi}{2} - \alpha\right) \tag{2.50}$$

  In Equation 2.50, the term r_2 represents the sphere of influence and α is the angle between this radius and dm. This last quantity is called the *missing distance*. To ensure that the spacecraft does not impact the planet's surface, the condition $dm > B$ must be respected. Here, B is the impact parameter, which corresponds to the missing distance when the periapsis radius is equal to the planet's one ($r_P = R_V$).

- *Outer Planet*

  When a spacecraft approaches an inner planet, it will anticipate it, since it is slower.

FlyBy

When approaching a celestial body, the condition $dm > B$ must be satisfied. If it is, three scenarios can arise:

- Capture: the spacecraft is drawn into the celestial body's sphere of influence and begins to follow a circular orbit around it;

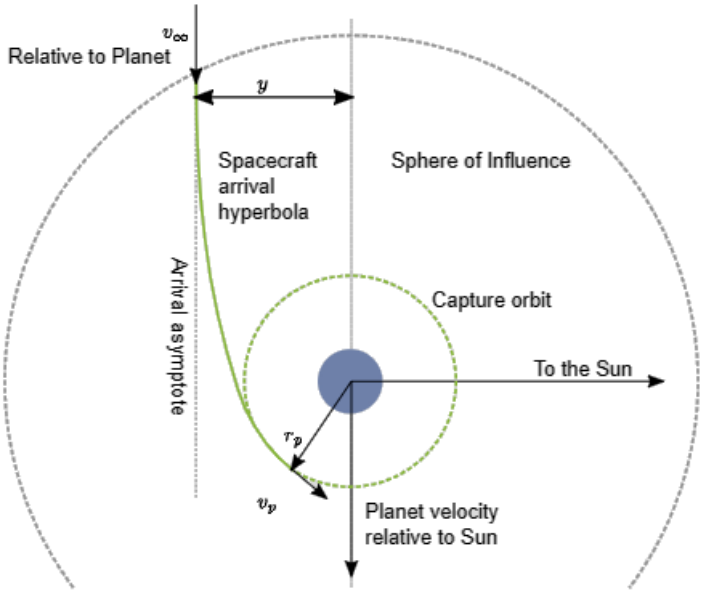

Figure 2.10: Arrival to an inner planet [26]

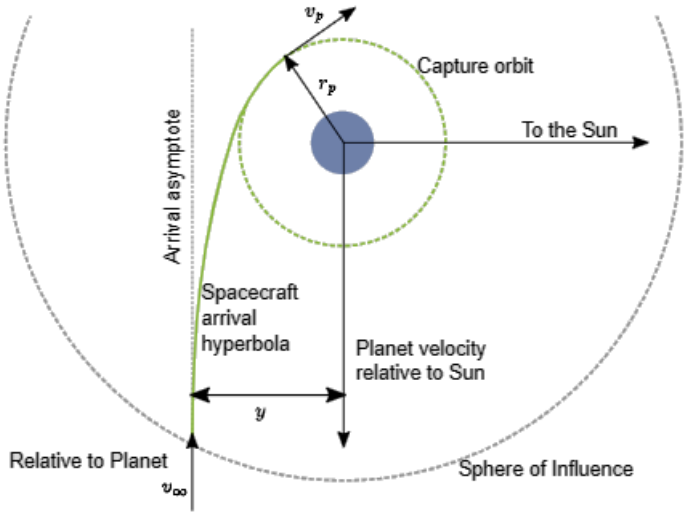

Figure 2.11: Arrival to an outer planet [26]

- Trailing-side flyby: the spacecraft performs a maneuver behind the celestial body, gaining velocity;
- Leading-side flyby: the spacecraft performs a maneuver in front of the celestial body, losing velocity.

Flyby is a maneuver employed in interplanetary missions. During a flyby, a spacecraft approaches a planet or moon and utilizes its gravity to modify its trajectory. In simpler terms, it can either gain speed or alter its direction.

- *Trailing-side Flyby*

  By performing a trailing-side flyby, the spacecraft can increase its trajectory's energy as it exits the celestial body's sphere of influence, all without relying on its propulsors.

  When examining Figure 2.12, it becomes evident that $v_{\infty,1}$ and $v_{\infty,2}$, the relative velocities of the orbit, share the same magnitude but differ in direction. By recalling the momentum equation, it is possible to demonstrate its increase:

$$\begin{cases} h_1 = V_1^s r_1 cos(\alpha_1) \\ h_2 = V_2^s r_2 cos(\alpha_2) \end{cases} \tag{2.51}$$

  As a result of this maneuver, $V_2 > V_1$ and $\alpha_2 < \alpha_1$. Therefor, $cos(\alpha_2) > cos(\alpha_1)$ and, as a consequence, $h_2 > h_1$.

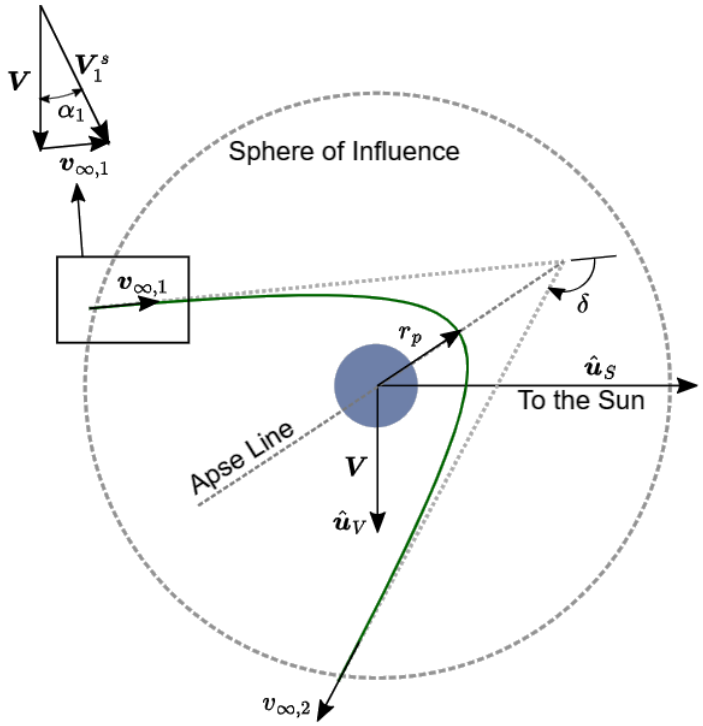

Figure 2.12: Trailing-side flyby [26]

- *Leading-side Flyby*

  On the other hand, by performing a trailing-side flyby, the spacecraft can decrease its trajectory's energy, without using its propulsors. Again, by recalling the momentum equation, it is possible to demonstrate its decrease.

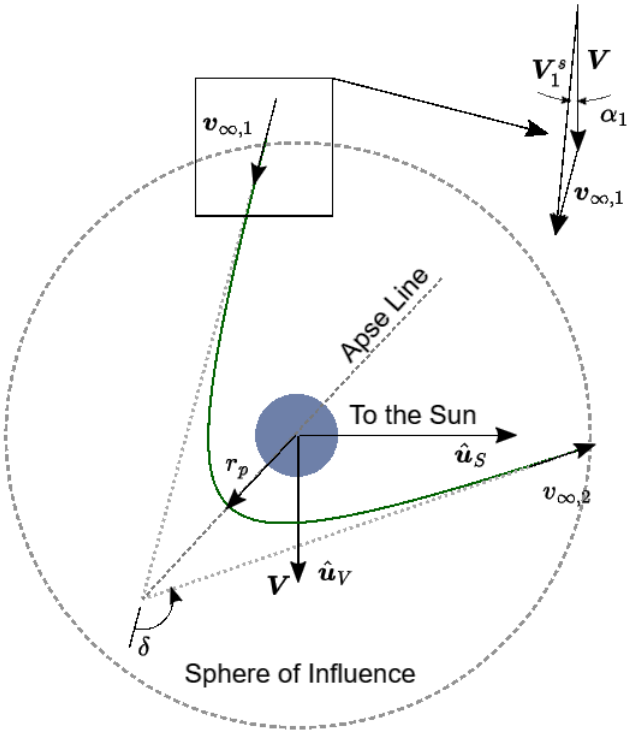

Figure 2.13: Leading-side flyby [26]

2.1.10 Lagrangian Points

Lagrangian points, named after Joseph-Louis Lagrange, are equilibrium points resulting from the interaction of the gravitational fields of two major bodies, of masses $m_1 > m_2$. Due to their unique properties, a third, smaller object, m, can remain stationary at these points with minimal propellant consumption [27].

Usually, the model used to describe these points is the Circular Restricted Three-Body Problem (CR3BP). This simplified model assumes that the orbits of the two major bodies are circular around their common center of mass and that the third body has a negligible mass compared to the other two. In such system, the equation of motion for the smaller body is:

$$\ddot{\vec{r}} + \vec{\omega} \wedge (\vec{\omega} \wedge \vec{r}) + 2\vec{\omega} \wedge \dot{\vec{r}} = \frac{1}{m}(\vec{F_1} + \vec{F_2}) \tag{2.52}$$

The terms on the left of Equation 2.52 represents the inertial, centripetal and Coriolis forces, while the terms on the right represent the forces applied by m_1 and m_2 on m. This equation can be rewritten in its three-component, non-dimensional form:

$$\begin{cases} \xi'' - \xi - 2\eta' = -(1-\mu)\frac{\xi+\mu}{\rho_1^3} - \mu\frac{\xi-(1-\mu)}{\rho_2^3} \\ \eta'' - \eta + 2\xi' = -(1-\mu)\frac{\eta}{\rho_1^3} - \mu\frac{\eta}{\rho_2^3} \\ \zeta'' = -(1-\mu)\frac{\zeta}{\rho_1^3} - \mu\frac{\zeta}{\rho_2^3} \end{cases} \tag{2.53}$$

Where $\mu = \frac{m_2}{M}$ is not a gravitational parameter, with $M = m_1 + m_2$, and $\{\xi, \eta, \zeta\}^T$ are the non-dimensional coordinates. Such equation can be solved numerically by converting it into a system of six Ordinary Differential Equations (ODEs) in six variables $x = \{\xi', \eta', \zeta', \xi'', \eta'', \zeta''\}^T$, which form the state vector.

To find the Lagrangian, or equilibrium, points, the components of relative velocity $\{\xi', \eta', \zeta'\}^T$ and acceleration $\{\xi'', \eta'', \zeta''\}^T$ must be nullify, so that every body stationed there remains motionless with respect to the reference frame. As shown in Figure 2.14, there exist five such points for any combination of two major bodies.

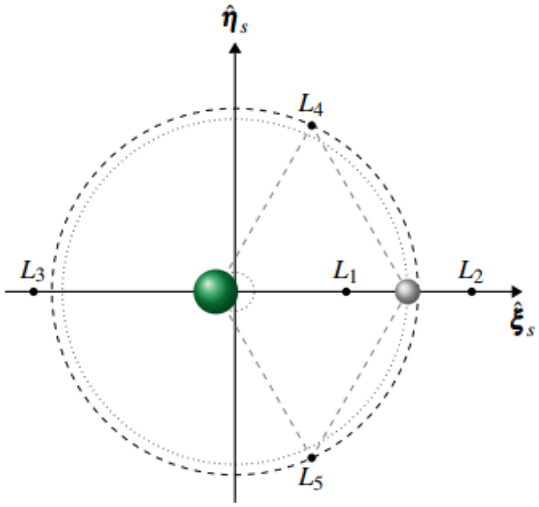

Figure 2.14: Lagrangian point in a Sun-Earth system [12]

To find their coordinates, it is necessary to define a potential function $\mathcal{U}$ and derive it with respect to the three non-dimensional coordinates. Therefor, starting from:

$$\mathcal{U} = \frac{1-\mu}{\rho_1} + \frac{\mu}{\rho_2} + \frac{1}{2}(\xi^2 + \eta^2) \tag{2.54}$$

The following system is obtained:

$$\begin{cases} \frac{\partial \mathcal{U}}{\partial \xi} = \xi'' - 2\eta' \\ \frac{\partial \mathcal{U}}{\partial \eta} = \eta'' + 2\xi' \\ \frac{\partial \mathcal{U}}{\partial \zeta} = \zeta'' \end{cases} \tag{2.55}$$

By setting these derivatives to zero, the coordinates of the Lagrangian points can be determined, which lie on the $\hat{\xi} - \hat{\eta}$ plane since the last equation is satisfied by imposing $\zeta = 0$. In the Sun-Earth system, these Lagrangian points are:

- By imposing $\eta = \zeta = 0$:
  - *L1*
    Known as the cis-Earth point, it lies on the line connecting the two major celestial bodies, before the smaller one. At the L1 point, the object's orbital period matches Earth's:

$$\begin{cases} \xi - (1-\mu)\frac{\xi+\mu}{\rho_1^3} - \mu\frac{\xi-(1-\mu)}{\rho_2^3} = 0 \\ \rho_1 + \rho_2 = 1 \end{cases} \quad \rightarrow \rho_2 \approx \sqrt[3]{\frac{\mu}{3}} \tag{2.56}$$

  - *L2*
    Known as the trans-Earth point, it lies on the line connecting the two major celestial bodies, beyond the smaller one. Similar to L1, the object's orbital period at L2 matches Earth's:

$$\begin{cases} \xi - (1-\mu)\frac{\xi+\mu}{\rho_1^3} - \mu\frac{\xi-(1-\mu)}{\rho_2^3} = 0 \\ \rho_1 - \rho_2 = 1 \end{cases} \quad \rightarrow \rho_2 \approx \sqrt[3]{\frac{\mu}{3}} \tag{2.57}$$

  - *L3*
    Known as the trans-Sun point, it lies on the line connecting the two major celestial bodies, before the larger one. At the L3 point, the object's orbital period also matches Earth's:

$$\begin{cases} \xi - (1-\mu)\frac{\xi+\mu}{\rho_1^3} - \mu\frac{\xi-(1-\mu)}{\rho_2^3} = 0 \\ \rho_2 - \rho_1 = 1 \end{cases} \quad \rightarrow \rho_2 \approx 2 \rightarrow \rho_1 \approx 1 \tag{2.58}$$

- By imposing $\rho_1 = \rho_2 = 1$:
  - *L4* and *L5*
    Known as the equilateral points, these are the only stable Lagrangian points, provided the mass ratio of the two bodies is sufficiently large:

$$\begin{cases} \xi - (1-\mu)\frac{\xi+\mu}{\rho_1^3} - \mu\frac{\xi-(1-\mu)}{\rho_2^3} = 0 \\ \eta - (1-\mu)\frac{\eta}{\rho_1^3} - \mu\frac{\eta)}{\rho_2^3} = 0 \end{cases} \rightarrow \begin{cases} \xi = \frac{1}{2} - \mu \\ \eta = \pm\frac{\sqrt{3}}{2} \end{cases} \tag{2.59}$$

While, as mentioned, L4 and L5 are stable Lagrangian points, L1, L2 and L3 are unstable, since even a small perturbation can cause an object to move away from them.

2.2 Equations of Motion

To describe the state evolution of a spacecraft, it is necessary to integrate a set of ODEs over time. These equations describe the spacecraft's changes in position, velocity, and mass:

$$\begin{aligned} \frac{d\vec{r}}{dt} &= \vec{V} \\ \frac{d\vec{V}}{dt} &= \vec{g} + \frac{\vec{T}}{m} + \frac{\vec{L}}{m} + \frac{\vec{D}}{m} + \vec{a}_p \\ \frac{dm}{dt} &= -\frac{T}{c} \end{aligned} \tag{2.60}$$

In the second equation, $\vec{T}$, $\vec{L}$ and $\vec{D}$ represent thrust, lift and drag respectively, while $\vec{a}_p$ the perturbations. Since the studied orbits are interplanetary transfers, the mission is located far from Earth's atmosphere, making the lift and drag terms negligible. The problem uses an heliocentric model, so the term $\vec{g}$ represents the gravitational acceleration generated by the central body, which is the Sun. Additionally, this mission does not consider the effects of perturbations, also making the term $\vec{a}_p$ negligible.

Finally, the last equation represents the loss of mass due to the propulsive phases.

2.2.1 Equations of Motion in Cartesian Coordinates

The equations of motion, as presented in Equation 2.60, can be reformulated in Cartesian coordinates. This involves considering the Cartesian components of position and velocity, denoted as $\vec{r} = \{x, y, z\}^T$ and $\vec{V} = \{V_x, V_y, V_z\}^T$:

$$
\begin{aligned}
\frac{dx}{dt} &= V_x \\
\frac{dy}{dt} &= V_y \\
\frac{dz}{dt} &= V_z \\
\frac{dV_x}{dt} &= -\frac{\mu}{r^{3/2}}x + \frac{\vec{T}}{m}\frac{\lambda_{V_x}}{\lambda_V} \\
\frac{dV_y}{dt} &= -\frac{\mu}{r^{3/2}}y + \frac{\vec{T}}{m}\frac{\lambda_{V_y}}{\lambda_V} \\
\frac{dV_z}{dt} &= -\frac{\mu}{r^{3/2}}z + \frac{\vec{T}}{m}\frac{\lambda_{V_z}}{\lambda_V} \\
\frac{dm}{dt} &= -\frac{T}{c}
\end{aligned}
\tag{2.61}
$$

The term λ_V represents the magnitude of the *prime vector* $\vec{\lambda}_V = \{\lambda_{V_x}, \lambda_{V_y}, \lambda_{V_z}\}$, which contains the costates of the velocity components.

Chapter 3

Mathematics and Code Implementation

3.1 Asteroids Selection

The initial step in defining this mission involves creating a database of all reachable asteroids. These asteroids are categorized into two groups: *numbered* and *non-numbered*. Numbered asteroids have well-defined physical characteristics and orbital parameters, whereas non-numbered asteroids have a certain degree of uncertainty due to the limited number of observations and available data [28][29]. Despite this, both categories are considered in this thesis, assuming the accuracy of the information provided by the JPL database [30]. This database was consulted in April 2024, filtering for NEAs that meet specific orbital conditions, as detailed in Table 3.1. These parameters were established to ensure the asteroid's orbit is close to Earth's and to guarantee a Minimum Orbital Intersection Distance (MOID) of less than 500 000 km.

	Value
Semi-major axis (a)	$0.97 \div 1.031$ au
Eccentricity (e)	< 0.1
Inclination (i)	$< 2°$

Table 3.1: Orbital conditions for the asteroids selection

In the second step, a two-impulse Hohmann transfer from Earth was considered to estimate the necessary ΔV, adhering to the condition of a maximum magnitude of $1\,\mathrm{km\,s^{-1}}$. Given the need for a plane change, a combined maneuver was employed:

$$\Delta V = \sqrt{\Delta V_1^2 + \Delta V_2^2 - 2V_1V_2\cos(\alpha\Delta i)} \tag{3.1}$$

The term α represents the fraction of the plane change performed during the first impulse, with the remainder executed during the second one. This approach reduces propellant usage, as the maneuver occurs farther from the central body and its gravitational pull. To ensure that 90% of the inclination change is always performed away from the Sun, an $\alpha = 0.9$ was used for asteroids closer to the Sun than Earth, and $\alpha = 0.1$ for those further away.

Out of the twenty remaining asteroids, ranked from the lowest to the highest estimated ΔV, the first two were selected for this mission. Their parameters are listed in Table 3.2.

	a [au]	e	i [°]	Ω [°]	ω [°]	ΔV $[kms^{-1}]$
2000 SG344	0.9773	0.0668	0.11	191.76	275.51	0.3512
2013 BS45	0.9915	0.0838	0.77	83.4	150.74	0.4405

Table 3.2: Orbital parameters of the chosen asteroids

Therefor, the mission begins at L2, where the mothership, carrying two probes, travels to the first asteroid, *2000 SG344*. The first probe is then released on its surface and the mission continues to the second asteroid, *2013 BS45*, where the remaining probe is also deployed.

3.2 Chosen Values

To define the orbital parameters of the starting point, L2, it is important to evaluate its distance from Earth, ρ_2, as shown in Equation 2.57. In the Sun-Earth system, the value of μ is defined as:

$$\mu = \frac{\mu_E}{\mu_S + \mu_E} \tag{3.2}$$

Given that $\rho_2 \approx 1.5 \times 10^6\,\text{km}$, the orbital parameters of L2 are the same as Earth's, except for the semi-major axis, which accounts for this additional distance, as detailed in Table 3.3.

	a [km]	e	i [°]	Ω [°]	ω [°]
$L2$	$1.496 \times 10^8 + \rho_2$	0.017	0	348.74	19.06

Table 3.3: Orbital parameters of L2

It is also important to note that the trans-Earth point moves in accordance with Earth, remaining aligned with both the planet and the Sun. Therefore, its initial velocity has been determined proportionally, based on Earth's.

The spacecraft has a total mass of 600 kg, with each probe weighting 25 kg. These values were chosen based on the studies Asteroid Reconnaissance Probes (ARProbes) and Geophysical Reconaissance Asteroid Surface Probe (GRASP) [31][32]. All the spacecraft's characteristic values are detailed in Table 3.4.

Total mass [kg]	*Probe mass* [kg]	*Thrust* [N]	I_{sp} [s]
600	25	0.1	3000

Table 3.4: Spacecraft's characteristics

3.2.1 Non-dimensionalizing Values

In such complex scenarios, it is easy to encounter different orders of magnitude, as seen in the Sun-Earth and Earth-L2 distances. To avoid numerical problems due to these disparities, every implemented value must be non-dimensionalized using the appropriate quantity. Consequently, in the code used for resolving the trajectory optimization problem, a series of non-dimensionalizing values has been considered:

$$\begin{aligned} L_{Adim} &= d_{SE} \\ m_{Adim} &= m_{sc} \\ \mu_{Adim} &= \mu_{Sun} \end{aligned} \tag{3.3}$$

Here, d_{SE} is the Sun-Earth distance, equal to 1 au $= 1.496 \times 10^8$ km, $m_{sc} = 600$ kg the spacecraft mass and $\mu_{Sun} = 1.327\,122 \times 10^{11}\,\mathrm{km^3\,s^{-2}}$ the gravitational parameter of the Sun. Any other non-dimensionalizing value result from a combination of these three:

$$\begin{aligned} V_{Adim} &= \sqrt{\frac{\mu_{Adim}}{L_{Adim}}} \\ t_{Adim} &= \frac{L_{Adim}}{V_{Adim}} \end{aligned} \tag{3.4}$$

Due to the very low inclination values of the targeted orbits, the length along the third axis is several orders of magnitude lower than the other two. To compensate for this difference, the non-dimensionalizing length for the *z-axis* has been multiplied by $\sin(2°)$. It is also important to note that, from this point forward, vectors will be presented in boldface to simplify the notation.

3.3 Differential Corrector

The scope of this thesis is to optimize interplanetary trajectories to ensure minimal propellant usage. Given the initial and final non-dimensional states, $\tilde{\boldsymbol{X}}(\tau_0)$ and $\tilde{\boldsymbol{X}}(\tau_f)$, it is possible to determine a path between the two. By selecting a reasonable initial guess for the initial state and integrating it over a specified duration, adjusting its initial parameters, the solution is found when the integrated final state closely matches the desired one. However, this approach lacks insight into how changes to the initial values affect the convergence, whether they improve or worsen it.

A more effective approach is the implementation of a Two Point Boundary Value Problem (TPBVP), which will be discussed later. The key concept is the understanding of how the initial state should be corrected in order to produce the desired final one, providing essential theoretical insights regarding the evolution over time of the associated state.

The discrepancy between the desired $\tilde{\boldsymbol{X}}^*(\tau_f)$ and the actual final state $\tilde{\boldsymbol{X}}(\tau_f)$, can be expressed as:

$$\delta\tilde{\boldsymbol{X}}(\tau_f) = \tilde{\boldsymbol{X}}(\tilde{\boldsymbol{X}}(\tau_0), \tau_f) - \tilde{\boldsymbol{X}}^*(\tilde{\boldsymbol{X}}^*(\tau_0), \tau_f) \tag{3.5}$$

The aim of the Differential Corrector (DC) is the elimination of such discrepancy. Therefor, it should exist a specific correction in the initial state, denoted as $\delta\tilde{\boldsymbol{X}}(\tau_0)$, able to produce the desired initial state:

$$\tilde{\boldsymbol{X}}^*(\tau_0) = \tilde{\boldsymbol{X}}(\tau_0) + \delta\tilde{\boldsymbol{X}}(\tau_0) \tag{3.6}$$

Therefor, Equation 3.5 can be expanded and linearized in the form:

$$\begin{aligned}
\delta\tilde{\boldsymbol{X}}(\tau_f) &= \tilde{\boldsymbol{X}}(\tilde{\boldsymbol{X}}(\tau_0), \tau_f) - \tilde{\boldsymbol{X}}^*(\tilde{\boldsymbol{X}}^*(\tau_0), \tau_f) \\
&= \tilde{\boldsymbol{X}}(\tilde{\boldsymbol{X}}(\tau_0) + \delta\tilde{\boldsymbol{X}}(\tau_0), \tau_f) - \tilde{\boldsymbol{X}}^*(\tilde{\boldsymbol{X}}^*(\tau_0), \tau_f) \\
&= \frac{\partial\tilde{\boldsymbol{X}}(\tau_f)}{\partial\tilde{\boldsymbol{X}}(\tau_0)}\delta\tilde{\boldsymbol{X}}(\tau_0) \\
&= \tilde{\boldsymbol{\Phi}}(\tau_f, \tau_0)\delta\tilde{\boldsymbol{X}}(\tau_0)
\end{aligned} \tag{3.7}$$

Based on the discrepancy obtained in the final state, this equation allows the calculation of the necessary correction to apply to the initial state. The term $\tilde{\boldsymbol{\Phi}}(\tau_f, \tau_0)$ represents the State Transition Matrix (STM), which encapsulates the relationship between the partial derivatives of the final state variables and those of the initial state, thereby creating a linear mapping between the initial and final states. Such matrix can be expressed in its non-dimensional, extended form, considering a generic instant τ instead of the final time τ_f:

$$\tilde{\mathbf{\Phi}}(\tau,\tau_0)=\begin{bmatrix} \frac{\partial x}{\partial x_0} & \frac{\partial x}{\partial y_0} & \frac{\partial x}{\partial z_0} & \frac{\partial x}{\partial \dot{x}_0} & \frac{\partial x}{\partial \dot{y}_0} & \frac{\partial x}{\partial \dot{z}_0} \\ \frac{\partial y}{\partial x_0} & \frac{\partial y}{\partial y_0} & \frac{\partial y}{\partial z_0} & \frac{\partial y}{\partial \dot{x}_0} & \frac{\partial y}{\partial \dot{y}_0} & \frac{\partial y}{\partial \dot{z}_0} \\ \frac{\partial z}{\partial x_0} & \frac{\partial z}{\partial y_0} & \frac{\partial z}{\partial z_0} & \frac{\partial z}{\partial \dot{x}_0} & \frac{\partial z}{\partial \dot{y}_0} & \frac{\partial z}{\partial \dot{z}_0} \\ \frac{\partial \dot{x}}{\partial x_0} & \frac{\partial \dot{x}}{\partial y_0} & \frac{\partial \dot{x}}{\partial z_0} & \frac{\partial \dot{x}}{\partial \dot{x}_0} & \frac{\partial \dot{x}}{\partial \dot{y}_0} & \frac{\partial \dot{x}}{\partial \dot{z}_0} \\ \frac{\partial \dot{y}}{\partial x_0} & \frac{\partial \dot{y}}{\partial y_0} & \frac{\partial \dot{y}}{\partial z_0} & \frac{\partial \dot{y}}{\partial \dot{x}_0} & \frac{\partial \dot{y}}{\partial \dot{y}_0} & \frac{\partial \dot{y}}{\partial \dot{z}_0} \\ \frac{\partial \dot{z}}{\partial x_0} & \frac{\partial \dot{z}}{\partial y_0} & \frac{\partial \dot{z}}{\partial z_0} & \frac{\partial \dot{z}}{\partial \dot{x}_0} & \frac{\partial \dot{z}}{\partial \dot{y}_0} & \frac{\partial \dot{z}}{\partial \dot{z}_0} \end{bmatrix} = \left[\begin{array}{c|c} \tilde{\mathbf{\Phi}}_{XX} & \tilde{\mathbf{\Phi}}_{XV} \\ \hline \tilde{\mathbf{\Phi}}_{VX} & \tilde{\mathbf{\Phi}}_{VV} \end{array}\right] \tag{3.8}$$

The subscript 0 indicates the initial time τ_0, while the generic time τ has been omitted in the numerator for clarity reasons. This is a 6x6 matrix composed of four 3x3 sub-matrices, where X and V represent, respectively, the position and velocity components. The STM, also known as the sensitivity matrix, measures how variations in the initial state affect the final one. Consequently, both the STM and the trajectory evolve over time in the same manner, with this evolution described by its own 36 ODEs:

$$\begin{aligned} \dot{\tilde{\mathbf{\Phi}}}(\tau,\tau_0) &= \frac{d}{d\tau}\tilde{\mathbf{\Phi}}(\tau,\tau_0) = \frac{d}{d\tau}\left(\frac{\partial \tilde{\boldsymbol{X}}}{\partial \tilde{\boldsymbol{X}}_0}\right) \\ &= \frac{\partial}{\partial \tilde{\boldsymbol{X}}_0}\left(\frac{d\tilde{\boldsymbol{X}}}{d\tau}\right) \\ &= \frac{\partial \dot{\tilde{\boldsymbol{X}}}}{\partial \tilde{\boldsymbol{X}}}\frac{\partial \tilde{\boldsymbol{X}}}{\partial \tilde{\boldsymbol{X}}_0} \\ &= \tilde{\boldsymbol{A}}(\tau)\tilde{\mathbf{\Phi}}(\tau,\tau_0) \end{aligned} \tag{3.9}$$

Where, to avoid burdening the notation, the shortenings $\tilde{\boldsymbol{X}}_f \triangleq \tilde{\boldsymbol{X}}(\tilde{\boldsymbol{X}}(\tau_0),\tau_f)$ and $\tilde{\boldsymbol{X}}_0 \triangleq \tilde{\boldsymbol{X}}(\tau_0)$ have been introduced. The evolution of the STM is, therefore, described by itself and the *Jacobian matrix* $\tilde{\boldsymbol{A}}(\tau)$, which contains all the first-order partial derivatives of a vector-valued function.

3.4 Single-shooting Procedure

As anticipated, this thesis implements a single-shooting procedure. This method involves adjusting certain initial conditions to achieve a specified set of end conditions, forming a TPBVP. It is a recursive method that iteratively targets the

desired final state while updating the initial conditions at each step, continuously checking for and correcting any undesired terminal deviations. It is important to note that not all initial quantities may be allowed to vary; some may need to remain fixed. Conversely, not all terminal quantities may be fixed; some may need to vary [33].

Therefor, the free-variable vector $\tilde{\boldsymbol{X}}_0 \in \mathbb{R}^{n\times 1}$ may include state elements such as positions and velocities, and is expressed as follows:

$$\tilde{\boldsymbol{X}}_0 = \{X_1, X_2, ..., X_n\}^T \tag{3.10}$$

The constraint vector, on the other hand, targets the desired final quantities. As a consequence, the differences between actual and desired final states are encapsulated in the complete constraint vector $\boldsymbol{\chi}(\tilde{\boldsymbol{X}}_f) \in \mathbb{R}^{m\times 1}$, in the form:

$$\boldsymbol{\chi}(\tilde{\boldsymbol{X}}_f) = \{\chi_1, \chi_2, ..., \chi_m\}^T = \begin{Bmatrix} x - x^* \\ y - y^* \\ z - z^* \\ \dot{x} - \dot{x}^* \\ \dot{y} - \dot{y}^* \\ \dot{z} - \dot{z}^* \end{Bmatrix} \tag{3.11}$$

The purpose of the correction method is, therefor, to search for a specific initial state $\tilde{\boldsymbol{X}}_0^*$ able to satisfy all the constraints, such that $\boldsymbol{\chi}(\tilde{\boldsymbol{X}}_f^*) = \boldsymbol{0}$. To determine how variations in the free-variable vector affect the constraint vector, a first-order Taylor expansion is performed. Thus, for a generic new variable state vector $\tilde{\boldsymbol{X}}$, the constraint vector can be defined as:

$$\boldsymbol{\chi}(\tilde{\boldsymbol{X}}) = \boldsymbol{\chi}(\tilde{\boldsymbol{X}}_0) + \frac{\partial \boldsymbol{\chi}(\tilde{\boldsymbol{X}}_0)}{\partial \tilde{\boldsymbol{X}}}(\tilde{\boldsymbol{X}} - \tilde{\boldsymbol{X}}_0) \tag{3.12}$$

In this equation, the Jacobian matrix $\tilde{\boldsymbol{J}}(\boldsymbol{\chi}(\tilde{\boldsymbol{X}}_0), \tilde{\boldsymbol{X}}) \in \mathbb{R}^{m\times n}$ is included once again. This matrix, as previously anticipated, is composed of the partial derivatives of the constraints with respect to the forward-in-time free-variable vector quantities:

$$\frac{\partial \boldsymbol{\chi}(\tilde{\boldsymbol{X}}_0)}{\partial \tilde{\boldsymbol{X}}} = \tilde{\boldsymbol{J}}(\boldsymbol{\chi}(\tilde{\boldsymbol{X}}_0), \tilde{\boldsymbol{X}}) = \begin{bmatrix} \frac{\partial \chi_1}{\partial \tilde{X}_1} & \frac{\partial \chi_1}{\partial \tilde{X}_2} & \cdots & \frac{\partial \chi_1}{\partial \tilde{X}_n} \\ \frac{\partial \chi_2}{\partial \tilde{X}_1} & \frac{\partial \chi_2}{\partial \tilde{X}_2} & \cdots & \frac{\partial \chi_2}{\partial \tilde{X}_n} \\ \vdots & \vdots & \ddots & \vdots \\ \frac{\partial \chi_m}{\partial \tilde{X}_1} & \frac{\partial \chi_m}{\partial \tilde{X}_2} & \cdots & \frac{\partial \chi_m}{\partial \tilde{X}_n} \end{bmatrix} \tag{3.13}$$

The Taylor expansion, as shown in Equation 3.12, can be expressed iteratively, where each subsequent step $r+1$ depends on the previous r-th one:

$$\boldsymbol{\chi}(\tilde{\boldsymbol{X}}_{r+1}) = \boldsymbol{\chi}(\tilde{\boldsymbol{X}}_r) + \frac{\partial \boldsymbol{\chi}(\tilde{\boldsymbol{X}}_r)}{\partial \tilde{\boldsymbol{X}}_{r+1}}(\tilde{\boldsymbol{X}}_{r+1} - \tilde{\boldsymbol{X}}_r) \tag{3.14}$$

Introducing the abbreviations $\boldsymbol{\chi}_r \triangleq \boldsymbol{\chi}(\tilde{\boldsymbol{X}}_r)$ and $\tilde{\boldsymbol{J}}(\boldsymbol{\chi}_r) \triangleq \tilde{\boldsymbol{J}}(\boldsymbol{\chi}(\tilde{\boldsymbol{X}}_r), \tilde{\boldsymbol{X}}_{r+1})$, if a solution exist, then $\boldsymbol{\chi}_{r+1} = \mathbf{0}$ and the iterative solution takes the form:

$$\boldsymbol{\chi_r} + [\tilde{\boldsymbol{J}}(\boldsymbol{\chi}_r)](\tilde{\boldsymbol{X}}_{r+1} - \tilde{\boldsymbol{X}}_r) = \mathbf{0} \tag{3.15}$$

By manipulating Equation 3.15, it is possible to isolate the initial state guess for the new iteration:

$$\tilde{\boldsymbol{X}}_{r+1} = \tilde{\boldsymbol{X}}_r - [\tilde{\boldsymbol{J}}(\boldsymbol{\chi}_r)]^{-1}\boldsymbol{\chi_r} \tag{3.16}$$

This expression, which ensures the next solution is as close as possible to the initial guess $\tilde{X}_r$ among the infinite possibilities, holds true if the number of variables equals the number of constraints, meaning $n = m$. However, if there are more variables than constraints, with $n > m$, Equation 3.16 takes the form:

$$\tilde{\boldsymbol{X}}_{r+1} = \tilde{\boldsymbol{X}}_r - [\tilde{\boldsymbol{J}}(\boldsymbol{\chi}_r)]^T[\tilde{\boldsymbol{J}}(\boldsymbol{\chi}_r)\tilde{\boldsymbol{J}}(\boldsymbol{\chi}_r)^T]^{-1}\boldsymbol{\chi_r} \tag{3.17}$$

Finally, a relaxation parameter, denoted as k_R, can be introduced to facilitate convergence, allowing for smaller corrections to be performed at each iteration. Therefore, these iterative methods take the following form:

$$\begin{cases} \tilde{\boldsymbol{X}}_{r+1} = \tilde{\boldsymbol{X}}_r - k_R[\tilde{\boldsymbol{J}}(\boldsymbol{\chi}_r)]^{-1}\boldsymbol{\chi_r} & \text{if } n = m \\ \tilde{\boldsymbol{X}}_{r+1} = \tilde{\boldsymbol{X}}_r - k_R[\tilde{\boldsymbol{J}}(\boldsymbol{\chi}_r)]^T[\tilde{\boldsymbol{J}}(\boldsymbol{\chi}_r)\tilde{\boldsymbol{J}}(\boldsymbol{\chi}_r)^T]^{-1}\boldsymbol{\chi_r} & \text{if } n > m \end{cases} \tag{3.18}$$

In this thesis's mission scenario, the number of variables and constraints is equal, so the first equation is used. The targeted orbit is defined by its CKP, with both the true anomaly (ν) and the mission duration (time of flight, tof) fixed. This approach ensures that not only the desired orbit is achieved, but also the exact position of the selected asteroid at the correct time. Conversely, if both parameters were left free, the orbit could be reached with minimal propellant usage by selecting the most convenient values for ν and tof. However, this would not account for the actual position of the asteroid, necessitating an additional phasing maneuver.

3.5 Implementation of the Code

All the concepts previously defined form the core of the Python code implemented to solve the trajectory optimization problem presented here. The code is structured into three main sections:

- *Adimensionalization:* this section is dedicated to defining the non-dimensionalizing parameters and their applications.
- *Functions:* this section defines the functions responsible for converting between Keplerian and Cartesian states.
- *Cartesian:* this final section outlines all the initial and final conditions, as well as the main functions. Of particular interest is the differential corrector function, which is paired with a precompiled *C++* integrator using the *Numbalsoda* library for its superior computational speed, stability and robustness [34]. This combination simultaneously exploits the superior speed and efficiency of *C++* and the user-friendly nature of Python.

Chapter 4

Optimal Control Theory

Trajectory optimization and Optimal Control Theory (OCT) are often used interchangeably, even though they represent distinct techniques for solving Optimal Control Problem (OCP). While the former aims to maximize or minimize a function and determine the associated variables, the latter is rooted in the Calculus of Variations (CoV). OCT leverages small variations to identify the maximum or minimum of a functional, that is to say a function of functions. Ultimately, OCT determines the control input that optimizes the aforementioned functional [35][36].

CoV was initially developed by Leonhard Euler in 1733, and its name is derived from his work *Elementa Calculi Variationum*. Over the subsequent years, other influential mathematicians, including Lagrange, made significant contributions to refining this theory. However, it was only in the 19^{th} century that Karl Weierstrass ultimately established a rigorous foundation for it [37][38][39].

OCT emerged around 1980, coinciding with the widespread adoption of digital computers. Since then, it has continued to evolve into the theory we recognize today [40].

4.1 Optimal Control Problem

An OCP seeks to maximize a specific merit index by determining the optimal control law from the set of admissible ones, which must satisfy all constraints for a trajectory that evolves within its dynamical model, transitioning from an initial to a final state. Such dynamical problem can be expressed as a set of first-order ODEs, in the general form:

$$\dot{\boldsymbol{x}}(t) = \boldsymbol{f}(\boldsymbol{x}(t), \boldsymbol{u}(t), t) \tag{4.1}$$

These equations are function of a state vector $\boldsymbol{x}(t)$, a control vector $\boldsymbol{u}(t)$ and an independent variable t, which represents the problem's time-dependence. Let's

denote the number of state variables as n, where $\boldsymbol{x}(t) \in \mathbb{R}^n$, and the number of control variables as m, where $\boldsymbol{u}(t) \in \mathbb{R}^m$.

In order to solve this problem, it is essential to define its boundary conditions. A problem in which these conditions are specified using the initial and final states is referred to as a TPBVP. In practical terms, these conditions are known as external and are evaluated at the initial instant t_0 and at the final one t_f. A trajectory problem may necessitate additional conditions related to intermediate time points, and all these boundary conditions are collectively encapsulated within a constraint vector:

$$\boldsymbol{\chi}(t) = \boldsymbol{f}(\boldsymbol{x}_0, \boldsymbol{x}_f, t_0, t_f) = \mathbf{0} \tag{4.2}$$

The OCP is evaluated using a merit index denoted by $\mathcal{J}$. This index takes into account the evolution over time of both the control and state vectors within the interval spanning from the initial to the final time:

$$\mathcal{J} = \boldsymbol{\varphi}(\boldsymbol{x}_0, \boldsymbol{x}_f, t_0, t_f) + \int_{t_0}^{t_f} [\boldsymbol{\Phi}(\boldsymbol{x}(t), \boldsymbol{u}(t), t)]dt \tag{4.3}$$

For a dynamic system, the merit index $\mathcal{J}$ is entirely determined by the control input $\boldsymbol{u}(t)$. The first function $\boldsymbol{\varphi}$ depends on the specific final state reached, while the integral of the function $\boldsymbol{\Phi}$ quantifies how the solution evolves over time to reach the final state from the initial one. Notably, since $\mathcal{J}$ is a functional, this optimization problem involves an unknown function rather than a simple variable.

From Equation 4.3, is possible to derive two distinct formulations: the Lagrange formulation, where $\boldsymbol{\varphi} = 0$, and the Mayer formulation, where $\boldsymbol{\Phi} = 0$. In this specific case, it will be used the latter approach. To further simplify the problem, it is necessary to introduce an augmented merit function $\mathcal{J}^*$ that quantifies how well the constraints and state variables are satisfied. The rationale behind this approach lies in the fact that solving a larger yet simplified problem is often easier than tackling a smaller but more intricate one. This simplification involves introducing two new quantities: the adjoint variables, contained in the adjoint vector $\boldsymbol{\lambda}(t) \in \mathbb{R}^n$, and the Lagrange multipliers $\boldsymbol{\mu} \in \mathbb{R}^m$. The augmented merit index is then expressed as follows:

$$\mathcal{J}^* = \boldsymbol{\varphi} + \boldsymbol{\mu}^T \boldsymbol{\chi} + \int_{t_0}^{t_f} [\boldsymbol{\Phi} + \boldsymbol{\lambda}^T (\boldsymbol{f} - \dot{\boldsymbol{x}})]dt \tag{4.4}$$

If the boundary conditions and state equations are satisfied, meaning that $\boldsymbol{\chi} = 0$ and $\boldsymbol{f} = \dot{\boldsymbol{x}}$, solving this augmented problem is equivalent to the resolution of the non-augmented one, since $\mathcal{J} = \mathcal{J}^*$. Within the integral, the time derivative of the state vector $\dot{\boldsymbol{x}}$ appears, which is unknown. To eliminate it, is possible to rewrite the term $-\boldsymbol{\lambda}^T \dot{\boldsymbol{x}}$ by integrating by parts:

$$\int_{t_0}^{t_f}(-\boldsymbol{\lambda}^T\dot{\boldsymbol{x}})dt = -\boldsymbol{\lambda}_f^T\boldsymbol{x}_f + \boldsymbol{\lambda}_0^T\boldsymbol{x}_0 + \int_{t_0}^{t_f}(\dot{\boldsymbol{\lambda}}^T\boldsymbol{x})dt \tag{4.5}$$

Then, is possible to substitute Equation 4.5 in 4.4, obtaining:

$$\mathcal{J}^* = \boldsymbol{\varphi} + \boldsymbol{\mu}^T\boldsymbol{\chi} + (\boldsymbol{\lambda}_0^T\boldsymbol{x}_0 - \boldsymbol{\lambda}_f^T\boldsymbol{x}_f) + \int_{t_0}^{t_f}(\boldsymbol{\Phi} + \boldsymbol{\lambda}^T\boldsymbol{f} - \dot{\boldsymbol{\lambda}}^T\boldsymbol{x})dt \tag{4.6}$$

This final equation reveals a quantity that will prove useful later: the system's Hamiltonian, denoted as $\mathcal{H}$, shown in Equation 4.7.

$$\mathcal{H} \triangleq \boldsymbol{\Phi} + \boldsymbol{\lambda}^T\boldsymbol{f} \tag{4.7}$$

It is also possible to obtain the first-order derivative of the augmented merit index. This derivative must be zero to ensure that the optimality conditions are satisfied and that $\mathcal{J}^*$ remains stationary at the optimal point:

$$\begin{aligned}
\delta\mathcal{J}^* = &\left(\frac{\partial\boldsymbol{\varphi}}{\partial t_0} + \boldsymbol{\mu}^T\frac{\partial\boldsymbol{\chi}}{\partial t_0} - \mathcal{H}_0\right)\delta t_0 + \\
&+ \left(\frac{\partial\boldsymbol{\varphi}}{\partial t_f} + \boldsymbol{\mu}^T\frac{\partial\boldsymbol{\chi}}{\partial t_f} + \mathcal{H}_f\right)\delta t_f + \\
&+ \left(\frac{\partial\boldsymbol{\varphi}}{\partial \boldsymbol{x}_0} + \boldsymbol{\mu}^T\frac{\partial\boldsymbol{\chi}}{\partial \boldsymbol{x}_0} + \boldsymbol{\lambda}_0^T\right)\boldsymbol{\delta x}_0 + \\
&+ \left(\frac{\partial\boldsymbol{\varphi}}{\partial \boldsymbol{x}_f} + \boldsymbol{\mu}^T\frac{\partial\boldsymbol{\chi}}{\partial \boldsymbol{x}_f} - \boldsymbol{\lambda}_f^T\right)\boldsymbol{\delta x}_f + \\
&+ \int_{t_0}^{t_f}\left[\left(\frac{\partial\mathcal{H}}{\partial\boldsymbol{x}} + \dot{\boldsymbol{\lambda}}^T\right)\boldsymbol{\delta x} + \frac{\partial\mathcal{H}}{\partial\boldsymbol{u}}\boldsymbol{\delta u}\right]dt, \quad j = 1, \ldots, n_p.
\end{aligned} \tag{4.8}$$

Each of the first four terms in Equation 4.8 is multiplied by a coefficient, respectively δt_0, δt_f, $\boldsymbol{\delta x}_0$, $\boldsymbol{\delta x}_f$, $\boldsymbol{\delta x}$ and $\boldsymbol{\delta u}$ and their nullification can provide new important equations:

- When $\delta t_0 = \delta t_f = 0$, two algebraic equations are produced, one at the initial time and another at the final. These equations are referred to as *transversality conditions*;
- When $\boldsymbol{\delta x}_0 = \boldsymbol{\delta x}_f = 0$, $2n$ algebraic equations are produced, one for each state at the initial and final bounds. These equations are referred to as the *optimality conditions*;
- When $\boldsymbol{\delta x} = \boldsymbol{\delta u} = 0$, n Euler-Lagrange ODEs are generated for the adjoint variables, along with m algebraic equations for the control.

4.1.1 Boundary Conditions for Optimality

When the multiplier coefficients δt_0, δt_f, $\boldsymbol{\delta x}_0$ and $\boldsymbol{\delta x}_f$ are set to zero, a system of n transversality equations and $2n$ optimality equations is obtained. These equations collectively establish the boundary conditions for optimality:

$$\frac{\partial \boldsymbol{\varphi}}{\partial t_0} + \boldsymbol{\mu}^T \frac{\partial \boldsymbol{\chi}}{\partial t_0} - \mathcal{H}_0 = 0 \tag{4.9}$$

$$\frac{\partial \boldsymbol{\varphi}}{\partial t_f} + \boldsymbol{\mu}^T \frac{\partial \boldsymbol{\chi}}{\partial t_f} + \mathcal{H}_f = 0 \tag{4.10}$$

$$\frac{\partial \boldsymbol{\varphi}}{\partial \boldsymbol{x}_0} + \boldsymbol{\mu}^T \frac{\partial \boldsymbol{\chi}}{\partial \boldsymbol{x}_0} - \boldsymbol{\lambda}_0^T = \mathbf{0} \tag{4.11}$$

$$\frac{\partial \boldsymbol{\varphi}}{\partial \boldsymbol{x}_f} + \boldsymbol{\mu}^T \frac{\partial \boldsymbol{\chi}}{\partial \boldsymbol{x}_f} + \boldsymbol{\lambda}_f^T = \mathbf{0} \tag{4.12}$$

In the context of transversality equations, if time does not appear in the function $\boldsymbol{\varphi}$ or in any constraint, then the Hamiltonian becomes zero, and the time becomes an optimization variable. However, if time is constrained and appears in the term $\boldsymbol{\chi}$, then the Hamiltonian remains unconstrained, and its value is influenced by the optimization process.

In the context of optimality equations, similar behavior is observed. If a state variable x_i does not appear in the function $\boldsymbol{\varphi}$ or any of the constraints, its corresponding adjoint variable λ_{x_i} becomes zero at the same point. However, if x_i is explicitly constrained, then λ_{x_i} remains unconstrained. These findings are more effectively illustrated in Table 4.1.

	Condition	**Result**
Transversality	t unconstrained	$\mathcal{H} = 0$
	t constrained	$\mathcal{H}$ free
Optimality	x_i unconstrained	$\lambda_{x_i} = 0$
	x_i constrained	λ_{x_i} free

Table 4.1: Rules for transversality and optimality conditions

4.1.2 Equations for Adjoint and Control Variables

As previously mentioned, from Equation 4.8, is possible to derive n Euler-Lagrange ODEs and m algebraic equations that describe the evolution of adjoint variables and controls over time. To obtain the ODEs, it is necessary to set the coefficient $\boldsymbol{\delta x}$ to zero:

$$\frac{d\boldsymbol{\lambda}}{dt} = -\left(\frac{\partial \mathcal{H}}{\partial \boldsymbol{x}}\right)^T \tag{4.13}$$

On the other hand, for the control, is necessary to nullify the coefficient $\boldsymbol{\delta u}$:

$$\left(\frac{\partial \mathcal{H}}{\partial \boldsymbol{u}}\right)^T = 0 \tag{4.14}$$

Pontryagin's Maximum Principle

In reference to Equation 4.14, generally, the control vector $\boldsymbol{u}$ may consist of one or more elements that are subject to specified admissibility limits, denoted as U. In this specific scenario, the focus will be solely on explicit constraints within the range $U_{min} \leq u \leq U_{max}$. The Pontryagin's Maximum Principle (PMP) states that when explicit admissibility constraints are present, the optimal control $\boldsymbol{u}^*$ for the desired trajectory is the one that, at each point along the trajectory, maximizes the Hamiltonian in that specific point. In the case of a minimization problem, the same concept is referred to as the Pontryagin's minimum Principle (PmP).

It is important to note that for this equation to remain valid, the Hamiltonian $\mathcal{H}$ cannot be linear or affine with respect to the bounded control. Consequently, is possible to identify two distinct cases:

$$\frac{\partial \mathcal{H}}{\partial u_i} = \begin{cases} k_{u_i} & \text{if } \mathcal{H} \text{ affine wrt } u_i \\ f\left(u_i\right) & \text{otherwise} \end{cases} \tag{4.15}$$

In the first case, if $\mathcal{H}$ is affine with respect to the bounded control u_i then, since such control cannot appear explicitly, the only solution is for the constant k_{u_i} to be null. The only alternative is to seek the remaining coefficients k_{u_i} provided from the derivation: if $k_{u_i} \neq 0$, then $\mathcal{H}$ is maximized by imposing $u_i = U_{i_max}$ if $k_{u_i} > 0$, or $u_i = U_{i_min}$ if $k_{u_i} < 0$. Such condition is referred to as *bang-bang control*.

4.2 Multi-Point Optimal Control Problem

Until now, only a TPBVP has been considered, where the boundary conditions are external. However, as previously mentioned, it is also possible to impose constraints on internal points along the trajectory, resulting in a Multi-Point Optimal Control Problem (MPOCP). In this case study, implementing such a problem would be necessary because a few fly-bys occur along the trajectory. Consequently, the trajectory could be divided into a number n_p of sub-intervals or arcs. These arcs would facilitate simplified convergence and enhance the code's robustness. Within each arc, the variables remain continuous, but they may exhibit discontinuities

at the junction points. Each j-th arc begins at a time $t_{(j-1)_+}$ and ends at $t_{(j)_-}$, spanning for an unknown duration Δt_j subject to optimization, as shown in Figure 4.1. Therefore, not every arc has the same duration, but this parameter depends solely on the optimum solution. However, implementing such an application would be challenging in this initial approach and, therefore, will be the focus of future studies.

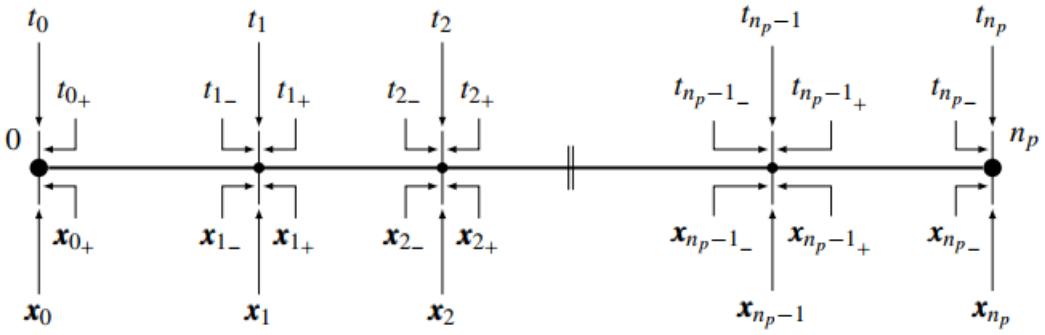

Figure 4.1: Schematic representation of a MPBVP

In a Multi-Point Boundary Value Problem (MPBVP), the constraint vector takes the form:

$$\boldsymbol{\chi}(\boldsymbol{x}_{(j-1)_+}, \boldsymbol{x}_{(j)_-}, t_{(j-1)_+}, t_{(j)_-}) = \mathbf{0}, \qquad j = 1, ..., n_p \tag{4.16}$$

Having considered not only the external boundaries, but also the internal ones. The merit index then $\mathcal{J}$ becomes:

$$\mathcal{J} = \boldsymbol{\varphi}\left(\boldsymbol{x}_{(j-1)_+}, \boldsymbol{x}_{(j)_-,}, t_{(j-1)_+}, t_{(j)_-}\right) + \sum_{j=1}^{n_p} \int_{t_{(j-1)_+}}^{t_{(j)_-}} \boldsymbol{\Phi}(\boldsymbol{x}(t), \boldsymbol{u}(t), t)dt \tag{4.17}$$

The augmented merit index $\mathcal{J}^*$ is again given by the sum of two terms: $\boldsymbol{\phi}$, depending on the values assumed for each arc and the entire trajectory, and the sum of integrals that quantify the evolution of the solution over time. However, in this case, $\boldsymbol{\Phi}$ specifically captures how the solution evolves arc-by-arc:

$$\mathcal{J}^* = \boldsymbol{\varphi} + \boldsymbol{\mu}^T\boldsymbol{\chi} + \sum_{j=1}^{n_p} \int_{t_{(j-1)_+}}^{t_{(j)-}} \left[\boldsymbol{\Phi} + \boldsymbol{\lambda}^T(\boldsymbol{f} - \dot{\boldsymbol{x}})\right] dt \tag{4.18}$$

Integrating by part, $\mathcal{J}^*$ becomes:

$$\mathcal{J}^* = \boldsymbol{\varphi} + \boldsymbol{\mu}^T \boldsymbol{\chi} + \sum_{j=1}^{n_p} \left(\boldsymbol{\lambda}_{(j-1)_+}^T \boldsymbol{x}_{(j-1)_+} - \boldsymbol{\lambda}_{(j)_-}^T \boldsymbol{x}_{(j)_-} \right) + \sum_{j=1}^{n_p} \int_{t_{(j-1)_+}}^{t_{(j)_-}} \left(\boldsymbol{\Phi} + \boldsymbol{\lambda}^T \boldsymbol{f} - \dot{\boldsymbol{\lambda}}^T \boldsymbol{x} \right) dt \tag{4.19}$$

Again, is possible to obtain the first order differentiation $\delta\mathcal{J}^*$ per each arc:

$$\begin{aligned}
\delta\mathcal{J}^* = & \left(\frac{\partial \boldsymbol{\varphi}}{\partial t_{(j-1)_+}} + \boldsymbol{\mu}^T \frac{\partial \boldsymbol{\chi}}{\partial t_{(j-1)_+}} - \mathcal{H}_{(j-1)_+} \right) \delta t_{(j-1)_+} + \\
& + \left(\frac{\partial \boldsymbol{\varphi}}{\partial t_{(j)_-}} + \boldsymbol{\mu}^T \frac{\partial \boldsymbol{\chi}}{\partial t_{(j)_-}} + \mathcal{H}_{(j)_-} \right) \delta t_{(j)_-} + \\
& + \left(\frac{\partial \boldsymbol{\varphi}}{\partial \boldsymbol{x}_{(j-1)_+}} + \boldsymbol{\mu}^T \frac{\partial \boldsymbol{\chi}}{\partial \boldsymbol{x}_{(j-1)_+}} + \boldsymbol{\lambda}_{(j-1)_+}^T \right) \boldsymbol{\delta x}_{(j-1)_+} + \\
& + \left(\frac{\partial \boldsymbol{\varphi}}{\partial \boldsymbol{x}_{(j)_-}} + \boldsymbol{\mu}^T \frac{\partial \boldsymbol{\chi}}{\partial \boldsymbol{x}_{(j)_-}} - \boldsymbol{\lambda}_{(j)_-}^T \right) \boldsymbol{\delta x}_{(j)_-} + \\
& + \sum_{j=1}^{n_p} \int_{t_{(j-1)_+}}^{t_{(j)_-}} \left[\left(\frac{\partial \mathcal{H}}{\partial \boldsymbol{x} + \dot{\boldsymbol{\lambda}}} \right) \boldsymbol{\delta x} + \frac{\partial \mathcal{H}}{\partial \boldsymbol{u}} \boldsymbol{\delta u} \right] dt, \quad j = 1, \ldots, n_p.
\end{aligned} \tag{4.20}$$

4.2.1 Boundary Conditions for Optimality and Equations for Adjoint and Control Variables

In the context of the MPBVP, it is more convenient to express the optimality and transversality conditions with respect to the j-th boundary itself. Consequently, the values are specified immediately before and after them, instead of considering the single arc:

$$\frac{\partial \boldsymbol{\varphi}}{\partial t_{j_+}} + \boldsymbol{\mu}^T \frac{\partial \boldsymbol{\chi}}{\partial t_{j_+}} - \mathcal{H}_{j_+} = 0, \quad j = 0, \ldots, n_p - 1 \tag{4.21}$$

$$\frac{\partial \boldsymbol{\varphi}}{\partial t_{j_-}} + \boldsymbol{\mu}^T \frac{\partial \boldsymbol{\chi}}{\partial t_{j_-}} + \mathcal{H}_{j_-} = 0, \quad j = 1, \ldots, n_p \tag{4.22}$$

$$\frac{\partial \boldsymbol{\varphi}}{\partial \boldsymbol{x}_{j_+}} + \boldsymbol{\mu}^T \frac{\partial \boldsymbol{\chi}}{\partial \boldsymbol{x}_{j_+}} + \boldsymbol{\lambda}_{j_+}^T = \boldsymbol{0}, \quad j = 0, \ldots, n_p - 1 \tag{4.23}$$

$$\frac{\partial \boldsymbol{\varphi}}{\partial \boldsymbol{x}_{j_-}} + \boldsymbol{\mu}^T \frac{\partial \boldsymbol{\chi}}{\partial \boldsymbol{x}_{j_-}} - \boldsymbol{\lambda}_{j_-}^T = \boldsymbol{0}, \quad j = 1, \ldots, n_p \tag{4.24}$$

On the contrary, the equations for the adjoint and control variables remain unaltered.

4.3 The Implemented Boundary Value Problem

The primary objective of this thesis is to optimize transfer trajectories within a TBP, providing an accurate description of its dynamics. The two main challenges in implementing a TPBVP are the inherent non-linearity of such a complex scenario and the numerical issues that may arise from using the indirect method. Therefore, it is of utmost importance to enhance the robustness of the code and mitigate the high sensitivity to variations in the initial conditions.

To address this issue, the TPBVP is converted into an augmented version. The new optimal initial state now includes both the previously defined one and the adjoint vector:

$$\boldsymbol{y}_0^* = \{(\boldsymbol{x}_0^*)^T \ (\boldsymbol{\lambda}_0^*)^T\}^T \tag{4.25}$$

If found, this optimal initial state enables reaching the desired final condition, $\boldsymbol{y}_f^*$, while satisfying all boundary conditions. The chosen numerical method is the single-shooting one, selected for its straightforward implementation, computational efficiency and speed.

For the indirect method, the general form of the complete set of ODEs is:

$$\dot{\boldsymbol{y}} = \boldsymbol{f}(\boldsymbol{y}(t), t) \tag{4.26}$$

However, as previously mentioned, the problem may include some constant values. Therefore, a new vector that accounts for them can be introduced:

$$\boldsymbol{z} = \{\boldsymbol{y}^T \ \boldsymbol{c}^T\}^T \tag{4.27}$$

Where $\boldsymbol{c}$ is the vector of the aforementioned constants. Thus, the set of ODEs becomes:

$$\dot{\boldsymbol{z}} = \frac{d\boldsymbol{z}}{dt} = \boldsymbol{f}(\boldsymbol{z}(t), t) \tag{4.28}$$

Where:

$$\begin{aligned} \dot{\boldsymbol{y}} &= \frac{d\boldsymbol{y}}{dt} \\ \dot{\boldsymbol{c}} &= \frac{d\boldsymbol{c}}{dt} = \boldsymbol{0} \end{aligned} \tag{4.29}$$

The new complete set of boundary conditions is:

$$\boldsymbol{\chi}(\boldsymbol{z}) = \boldsymbol{0} \tag{4.30}$$

To achieve the desired final conditions, the single-shooting method must determine the optimal initial state $\boldsymbol{q}_0^*$ while ensuring that $\boldsymbol{\chi}(\boldsymbol{q}^*) = \boldsymbol{0}$. To begin this

iterative process, an initial guess vector, $\boldsymbol{q}_r = \boldsymbol{z}_0$, must be defined. Then, using a first-order Taylor expansion, the boundary conditions at the next iteration can be expressed as a function of the previous one:

$$\boldsymbol{\chi}(\boldsymbol{q}_{r+1}) = \boldsymbol{\chi}(\boldsymbol{q}_r) + \frac{\partial \boldsymbol{\chi}(\boldsymbol{q}_r)}{\partial \boldsymbol{q}_{r+1}}(\boldsymbol{q}_{r+1} - \boldsymbol{q}_r) \tag{4.31}$$

In this context, the Jacobian matrix is again present, indicating how small changes in $\boldsymbol{q}$ affect the problem and, therefore, how to correct the guess after each iteration. Introducing the notations $\boldsymbol{\chi}_r = \boldsymbol{\chi}(\boldsymbol{q}_r)$ and $\boldsymbol{J}(\boldsymbol{\chi}_r) = \boldsymbol{J}(\boldsymbol{\chi}(\boldsymbol{q}_r), \boldsymbol{q}_{r+1})$, if a solution exists, then $\boldsymbol{\chi}_{r+1} = \mathbf{0}$, and the iterative solution takes the form:

$$\boldsymbol{\chi}_r + [\boldsymbol{J}(\boldsymbol{\chi}_r)](\boldsymbol{q}_{r+1} - \boldsymbol{q}_r) = \mathbf{0} \tag{4.32}$$

Consequently, for the next iteration:

$$\boldsymbol{q}_{r+1} = \boldsymbol{q}_r - [\boldsymbol{J}(\boldsymbol{\chi}_r)]^{-1}\boldsymbol{\chi}_r \tag{4.33}$$

Previously, the Jacobian matrix was computed using the introduction of a STM. However, in this particular case, it is simply approximated using the forward finite-difference methods as follows:

$$\boldsymbol{J}(\boldsymbol{\chi}_r) = \frac{\tilde{\boldsymbol{\chi}}_r - \boldsymbol{\chi}_r}{\Delta} \tag{4.34}$$

Where $\tilde{\boldsymbol{\chi}}_r$ represents the perturbation of each free-variable element of the vector $\boldsymbol{q}$ and $\Delta = 1 \times 10^{-7}$.

Given the problem under analysis, it is evident that the current TPBVP is governed by the following system:

$$\dot{\boldsymbol{z}} = \boldsymbol{f}(\boldsymbol{z}(t), t) \tag{4.35}$$

Its integration is conducted with the implementation of an implicit multi-step numerical method with, based on the Adams-Moulton formulations, variable step size and order [41][42].

Equation 4.33 holds true, in the form:

$$\boldsymbol{z}_{r+1} = \boldsymbol{z}_r - k_1[\boldsymbol{J}(\boldsymbol{\chi}_r)]^{-1}\boldsymbol{\chi}_r \tag{4.36}$$

Here, k_1 represents the relaxation parameter, first introduced in Chapter 3. Typically, lower values of k_1 are preferred for greater precision, such as for initial guesses. As the solution approaches the optimal one, higher values of k_1 can be used.

Another step to enhance the robustness of the method is the application of a control on the successive error relative to the previous one:

$$E_{max,r+1} < k_2 E_{max,r} \tag{4.37}$$

Here, k_2 is another relaxation parameter. Its purpose is to help the initial step of the iterative process to converge, even if the first few steps increase the maximum error while establishing the correct optimality direction. If the error becomes too high and Equation 4.37 is not satisfied, a bisection method is applied to the correction up to five times. If convergence is still not achieved, the process is automatically stopped as it is unable to converge from the selected initial solution.

4.4 OCT for Spacecraft Trajectory Optimization

In this specific scenario, the system being optimized describes the dynamics of a spacecraft performing an interplanetary transfer within a heliocentric TBP. Therefore, from Equation 2.60, by omitting the terms related to perturbations, lift, and drag, the following set of ODEs is obtained:

$$\begin{aligned} \frac{d\boldsymbol{r}}{dt} &= \boldsymbol{V} \\ \frac{d\boldsymbol{V}}{dt} &= \boldsymbol{g} + \frac{\boldsymbol{T}}{m} \\ \frac{dm}{dt} &= -\frac{T}{c} \end{aligned} \tag{4.38}$$

The purpose of applying OCT is to determine the control law $\boldsymbol{u}^*(t)$ that maximizes the spacecraft's final mass after each maneuver. For the merit index, the preferred formulation is the Mayer form, where $\boldsymbol{\Phi} = 0$. Therefore, the merit index is simply the value of the final mass:

$$\mathcal{J} = \boldsymbol{\varphi} = m_f \tag{4.39}$$

The state vector consists of the orbit's CKP and the mass m:

$$\boldsymbol{x}_k = \{a, e, i, \Omega, \omega, \nu, m\}^T \tag{4.40}$$

Which can be converted in Cartesian coordinates:

$$\boldsymbol{x}_c = \{x, y, z, V_x, V_y, V_z, m\}^T \tag{4.41}$$

Additionally, each state variable is paired with its corresponding adjoint variable, resulting in the augmented state vector:

$$\boldsymbol{y} = \{x, y, z, V_x, V_y, V_z, m, \lambda_x, \lambda_y, \lambda_z, \lambda_{V_x}, \lambda_{V_y}, \lambda_{V_z}, \lambda_m\}^T \tag{4.42}$$

By recalling Equation 4.7 and applying Mayer formulation, is possible to derive the Hamiltonian as shown in Equation 4.43.

$$\begin{aligned}\mathcal{H} = \boldsymbol{\lambda}^T \boldsymbol{f} = \sum_{i=1}^{2n} \lambda_i f_i = \lambda_x V_x + \lambda_y V_y + \lambda_z V_z \\ + \lambda_{V_x}\left[-\frac{\mu}{r^{3/2}}x + \frac{T}{m}\frac{\lambda_{V_x}}{\lambda_V}\right] \\ + \lambda_{V_y}\left[-\frac{\mu}{r^{3/2}}y + \frac{T}{m}\frac{\lambda_{V_y}}{\lambda_V}\right] \\ + \lambda_{V_z}\left[-\frac{\mu}{r^{3/2}}z + \frac{T}{m}\frac{\lambda_{V_z}}{\lambda_V}\right] \\ - \lambda_m \frac{T}{m}\end{aligned} \tag{4.43}$$

Here, $\boldsymbol{\lambda}_V$ refers to the prime vector as defined in Equation 2.61. Equation 4.43 can be expressed in a compact form by grouping all terms that multiply the thrust-to-mass ratio into what is known as the *switching function* $\mathcal{S}_\mathcal{F}$.

$$\mathcal{H} = \boldsymbol{\lambda}_x^T \boldsymbol{V} + \boldsymbol{\lambda}_V^T \left(-\mu \frac{\boldsymbol{x}}{r^{3/2}}\right) + T\mathcal{S}_\mathcal{F} \tag{4.44}$$

Where:

$$\mathcal{S}_\mathcal{F} = \frac{\boldsymbol{\lambda}_V^T}{m}\frac{\boldsymbol{T}}{T} - \frac{\lambda_m}{c} \tag{4.45}$$

The control vector $\boldsymbol{u}(t)$ consists of the magnitude of the thrust vector T and its direction. According to the PMP, the optimal control $\boldsymbol{u}^*$ that maximizes the merit index for the trajectory also maximizes the Hamiltonian, which is linear with respect to the control. This allows for the implementation of bang-bang control. Consequently, when $\mathcal{S}_\mathcal{F} > 0$, the thrust should be maximized ($T = T_{max}$), and when $\mathcal{S}_\mathcal{F} < 0$, the thrust should be zero ($T = 0$). The switching between positive and negative values of the switching function results in the presence of thrust and coasting arcs.

Based on Lawden's work, an important result regarding the thrust direction can be derived: S_F is maximized when the thrust is directed parallel to the primer vector $\boldsymbol{\lambda_V}$ [43]. Consequently, the switching function can be expressed in its scalar form as follows:

$$\mathcal{S}_\mathcal{F} = \frac{\lambda_V^T}{m} - \frac{\lambda_m}{c} \tag{4.46}$$

The thrust direction is determined by an in-plane angle, α_T, and an out-of-plane angle, β_T. Therefore, the thrust vector $\boldsymbol{T}$ can be decomposed into its three components using these two angles:

$$\boldsymbol{T} = T \begin{Bmatrix} cos\alpha_T cos\beta_T \\ sin\alpha_T cos\beta_T \\ sin\beta_T \end{Bmatrix} \tag{4.47}$$

The optimal values for these thrust angles are obtained by deriving the Hamiltonian with respect to the angles themselves:

$$\begin{aligned} \frac{\partial \mathcal{H}}{\partial \alpha_T} &= -\lambda_{V_x} sin\alpha_T + \lambda_{V_y} cos\alpha_T = 0 \\ \frac{\partial \mathcal{H}}{\partial \beta_T} &= \lambda_{V_z} cos\beta_T - (\lambda_{V_x} cos\alpha_T + \lambda_{V_y} sin\alpha_T) sin\beta_T = 0 \end{aligned} \tag{4.48}$$

As a result, the optimal directions are reported in Equation 4.49.

$$\begin{aligned} cos\alpha_T cos\beta_T &= \frac{\lambda_{V_x}}{\lambda_V} \\ sin\alpha_T cos\beta_T &= \frac{\lambda_{V_y}}{\lambda_V} \\ sin\beta_T &= \frac{\lambda_{V_z}}{\lambda_V} \end{aligned} \tag{4.49}$$

Therefor, the optimal directions can be easily computed and the augmented TPBVP is completely defined by finding the adjoint variables, via integration from Equation 4.13.

Chapter 5

Results

The objective of this thesis is to optimize interplanetary transfers between NEAs that satisfy specific orbital criteria. The mission commences at the Lagrangian point L2, where the mother-ship initiates its first transfer to the asteroid 2000 SG344. Upon deploying the first probe on its surface, the mission continues to the asteroid 2013 BS45, where the second probe is released. These transfers occur within a heliocentric TBP framework

The goal of the optimization is to minimize propellant usage, which translates to maximizing the spacecraft's final mass, enabling the application of the PMP. The potential trajectories are therefor analyzed using an indirect method within a TPBVP, employing a bang-bang control law represented by the switching function.

Consequently, the state vector comprises the orbit's CKP and the spacecraft's mass. The dynamics of the mother-ship during the interplanetary transfer are described by a set of ODEs. The problem is augmented by introducing the corresponding adjoint variables, and the merit index is implemented using the Mayer formulation. The optimization problem, therefor, focuses on finding the optimal costates that enable the spacecraft to adjust its trajectory, directing its thrust in the preferred direction while meeting all imposed constraints. These boundary conditions are defined by the initial and final states, as well as the spacecraft and engine characteristics. The mission duration is fixed, and the target orbit is achieved through the single-shooting procedure.

This optimization enables efficient navigation between NEAs, ensuring minimal propellant usage and serving as a valuable tool for future mission designs.

5.1 Interplanetary Transfer from L2 to 2000 SG344

The first phase of the mission involves transferring from the starting point L2 to the first asteroid, 2000 SG344, as detailed in Section 3.

The initial and final CKP are known from their Ephemerides. However, to define the precise starting and arrival points, it is necessary to determine their true anomalies, ν. The departure is hypothesized to occur on the 24^{th} January 2026, with L2's true anomaly being 19.058 2°. The arrival point is arbitrarily chosen at a true anomaly of 120° for 2000 SG344. If the time of flight (tof) is left unrestricted, the code converges on a solution that minimizes propellant consumption without considering the asteroid's actual position, necessitating a phasing maneuver later. Therefore, it is crucial to impose a tof that accounts for the real position of 2000 SG344. The precise values considered for ν, the arrival date, and tof are provided in Table 5.1.

Date of Arrival	ν [°]	tof [days]
03^{rd} Jun 2026	120.3086	131
22^{th} May 2027	120.2334	483

Table 5.1: Chosen ν and tof for the arrival at 2000 SG344

For the first iteration, the minimum value of tof was selected, meaning a transfer duration of 131 days. The resulting trajectory is illustrated in Figure 5.1.

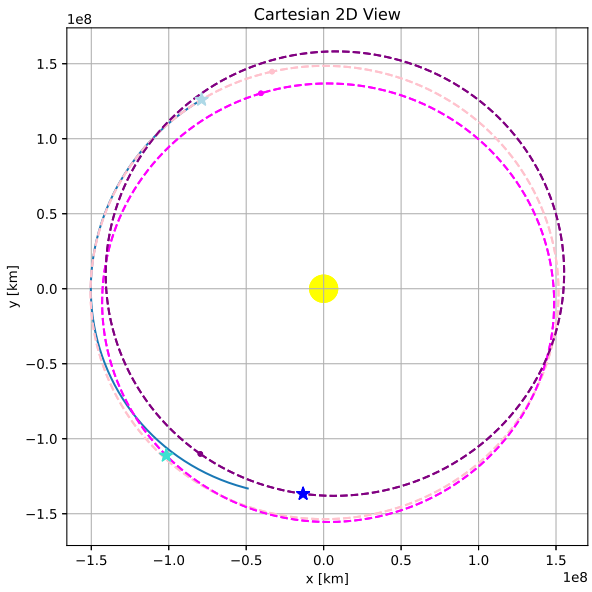

Figure 5.1: Plane View - 131 days

The starting point is located on the pink orbit, marked by a light-blue star, while

the final point is on the magenta orbit, indicated by a turquoise star. This scenario exemplifies non-convergence, as the trajectory does not terminate at the arrival point. Although the mother-ship can reach the desired final position, the time of flight is insufficient. Consequently, the $\mathcal{S}_{\mathcal{F}}$ remains consistently negative or, in an alternative attempt, always positive as it tries to complete a full revolution around the sun. However, due to the limited mission time, this maneuver is unfeasible.

The second instance when asteroid 2000 SG344 reaches a true anomaly of 120° occurs 483 days after the initial departure date. Consequently, the tof has been adjusted, setting the arrival date to 22^{th} May 2027.

With a plausible mission time established, the next step is to define the adjoint variables necessary to achieve the desired final state. As discussed in Section 4, the state vector consists of the CKP expressed in Cartesian coordinates and the spacecraft's mass. Consequently, each component has a corresponding costate, denoted as λ. Therefore, the initial guess vector includes three adjoint variables for the mother-ship's position (λ_x, λ_y and λ_z), three for its velocity (λ_{V_x}, λ_{V_y} and λ_{V_z}), and one for its mass (λ_m).

Since the goal of the optimization is to maximize the final mass, it is convenient to set the initial value of its costate to $\lambda_m = 1$. To determine the correct values for the remaining adjoint variables, it is crucial to understand their influence on the resulting trajectory. Therefore, by applying Equation 4.13, is possible to derive the n Euler-Lagrange equations for the costates:

$$\begin{aligned}
\frac{d\lambda_x}{dt} &= \left(\frac{\mu}{r^{3/2}} - \frac{3\mu}{r^{5/2}}x^2\right)\lambda_{V_x} - \frac{3\mu}{r^{5/2}}x(\lambda_{V_y}y + \lambda_{V_z}z) \\
\frac{d\lambda_y}{dt} &= \left(\frac{\mu}{r^{3/2}} - \frac{3\mu}{r^{5/2}}y^2\right)\lambda_{V_y} - \frac{3\mu}{r^{5/2}}y(\lambda_{V_x}x + \lambda_{V_z}z) \\
\frac{d\lambda_z}{dt} &= \left(\frac{\mu}{r^{3/2}} - \frac{3\mu}{r^{5/2}}z^2\right)\lambda_{V_z} - \frac{3\mu}{r^{5/2}}z(\lambda_{V_x}x + \lambda_{V_y}y) \\
\frac{d\lambda_{V_x}}{dt} &= -\lambda_x \\
\frac{d\lambda_{V_y}}{dt} &= -\lambda_y \\
\frac{d\lambda_{V_z}}{dt} &= -\lambda_z \\
\frac{d\lambda_m}{dt} &= T\frac{\lambda_V}{m^2}
\end{aligned} \tag{5.1}$$

From Equation 5.1, it is clear that the derivatives of the prime vector components depend on the position adjoint variables. Referring to Equation 4.46, since the second term is fixed, only the first one can vary. Consequently, the value of the switching function is linked to the prime vector itself. This implies that higher values in the position components result in a higher $\boldsymbol{\lambda}_V$, leading to a more positive

$\mathcal{S}_{\mathcal{F}}$ and, therefore, longer thrust arcs.

Conversely, Equation 4.49 demonstrates how the initial velocity adjoint variables affect the optimal thrust direction. As a result, higher values in these components lead to greater angles diverging from the trajectory tangent, resulting in higher values of α and β, and thus, showing a steering tendency.

Therefore, after implementing an initial guess for the optimal costates, it is crucial to monitor the trajectory behavior to progressively adjust their values. By following this strategy, convergence for the first segment of the mission was achieved in 207 iterations, using the following initial guess:

$$\boldsymbol{\lambda} = \{0.3, 0.3, 0.3, 0.0015, 0.0015, 0.0015, 1\}^T \tag{5.2}$$

This resulted in the optimal initial guess:

$$\begin{aligned}\boldsymbol{\lambda}_{opt} =&\{-4.5786e-01, 7.1732e-01, -8.9854e-02,\\ &-1.0274e+00, -5.3346e-01, -1.6516e-02, 9.4008e-01\}^T\end{aligned} \tag{5.3}$$

By implementing $\boldsymbol{\lambda}_{opt}$, convergence is achieved in 135 iterations, with the final results illustrated through a series of diagrams.

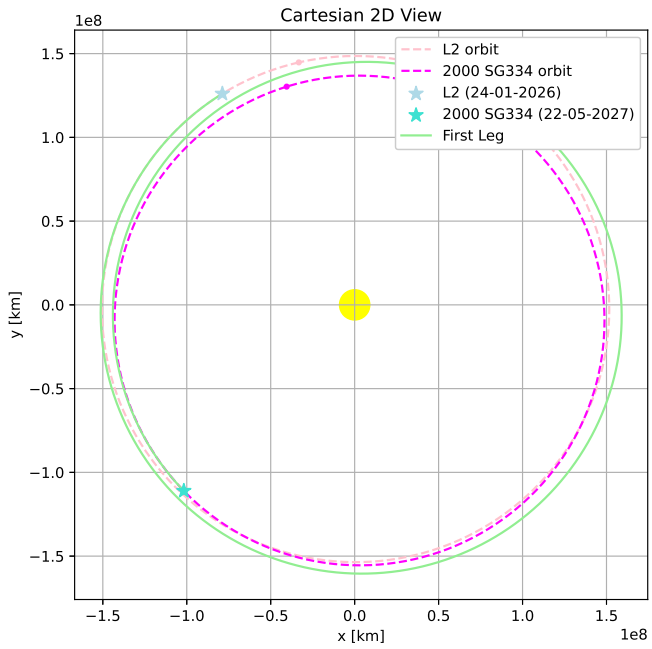

Figure 5.2: First Leg 2D View - 483 days

Figure 5.2 illustrates the initial segment of the trajectory in a Cartesian $2D$ view, clearly showing the arrival at the desired final position after 483 days. In contrast, Figure 5.3 presents the same trajectory in a Cartesian $3D$ view, offering a more comprehensive perspective. Notably, in this diagram, the z-axis is scaled differently to enhance the visibility of the various inclinations.

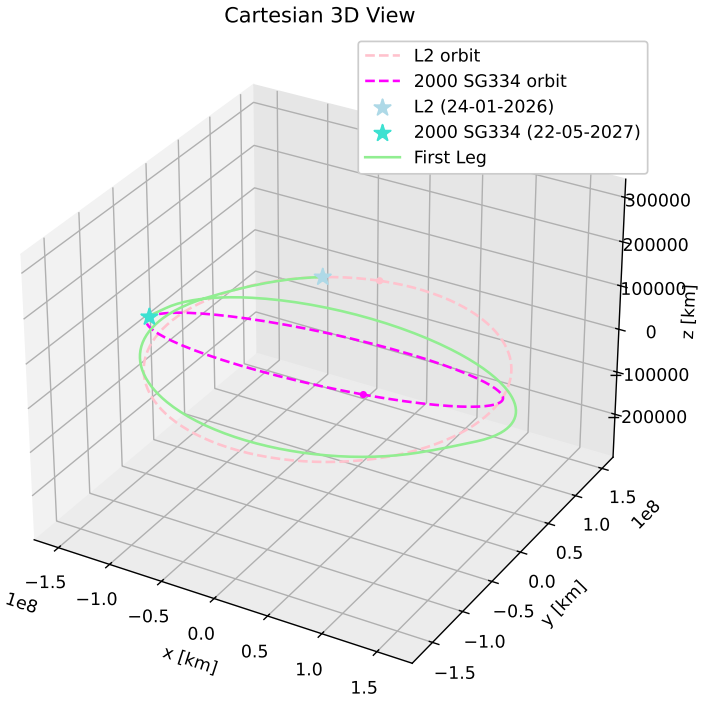

Figure 5.3: First Leg 3D View - 483 days

Figure 5.4 presents the CKP followed by the trajectory, enabling verification of the initial and final values. Notably, the trends on the right side are of particular interest. The $\mathcal{S}_{\mathcal{F}}$ depict three thrust arcs, while the mass trend indicates the corresponding propellant consumption. Conversely, during the coasting arcs, the total mass remains constant. Throughout the first thrust arc, the semi-major axis, eccentricity, and inclination experience an initial increase. To achieve these results, the thrust is directed with an initial negative value in both the in-plane angle (β) and the out-of-plane angle (α), thereby propelling the spacecraft forward and towards the higher inclination of the desired orbit. During the second and third thrust arcs, the eccentricity and inclination increase again, while the semi-major

axis decreases, aligning the final values with those of the first asteroid.

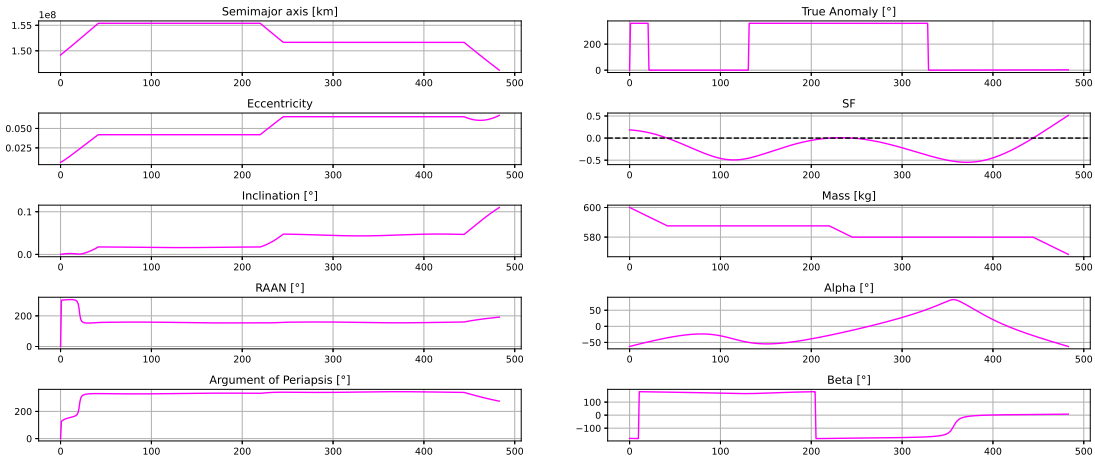

(a) a, e, i, Ω, ω **(b)** ν, $\mathcal{S}_{\mathcal{F}}$, m, α, β

Figure 5.4: First Leg - Trends over tof [days]

Once the initial convergence is achieved, obtaining new results for different values of true anomaly and time of flight becomes straightforward. In other words, if convergence is found for a specific value of ν and its corresponding tof, the optimal initial guess obtained can be used to easily find a new solution for slightly altered desired true anomaly and time of flight. This technique transforms the first convergence into a key to access the entire final orbit and, the same procedure, can also be applied to the starting one.

Suppose the mission objective has changed: instead of reaching asteroid 2000 SG344 at a true anomaly of 120.233 4° in 483 days, the new target is to reach it at 110.564 0° in 473 days. Utilizing the previously determined optimal initial guess, as shown in Equation 5.3, convergence for the updated scenario is now achieved in just 142 iterations, with the new $\boldsymbol{\lambda}_{opt}$ as follows:

$$\begin{aligned}\boldsymbol{\lambda}_{opt} =\{&-5.2259e-01, 7.4353e-01, -1.1388e-01,\\ &-1.1123e+00, -5.3093e-01, -3.6460e-02, 9.3647e-01\}^T\end{aligned} \tag{5.4}$$

As a result, identifying the most efficient solution among all the options becomes relatively straightforward.

5.2 Interplanetary Transfer from 2000 SG344 to 2013 BS45

The second leg of the mission involves a transfer between the two selected asteroids, following the release of the first probe. Consequently, the initial point for this maneuver aligns with the final one from the previous phase. This point is automatically calculated by the code and reinserted, rather than being manually input, to ensure continuity.

For the arrival point, various combinations of time of flight and true anomaly ν were initially considered. However, due to a larger inclination difference in this phase, the code faced challenges in achieving convergence. Consequently, the true anomaly was selected to minimize the shift along the z-axis, settling on a value of 30°, where the two orbits nearly intersect. Table 5.2 shows the available arrival dates.

Date of Arrival	ν [°]	tof [days]
27^{th} Mar 2028	29.8856	311
23^{th} Mar 2029	30.3139	671

Table 5.2: Chosen ν and tof for the arrival at 2013 BS45

Once again, the optimal initial guess was determined by monitoring the trajectory's evolution. Imposing the first hypothesized arrival date resulted in a consistently positive $\mathcal{S}_{\mathcal{F}}$, indicating that the final point couldn't be reached within the short time-frame. Therefore, the selected parameters were $\nu = 30.3139$ with a $tof = 671$. Convergence was achieved in 308 iterations using the following initial guess:

$$\boldsymbol{\lambda} = \{0.28, 0.28, 0.28, 0.045, 0.045, 0.045, 1\}^T \tag{5.5}$$

This resulted in the optimal initial guess:

$$\begin{aligned}\boldsymbol{\lambda}_{opt} =&\{5.3568e-01, 1.0760e+00, 1.1021e-01,\\ &-4.3459e-01, 1.0359e+00, -1.8466e-01, 8.4039e-01\}^T\end{aligned} \tag{5.6}$$

Figures 5.5 and 5.6 illustrate the trajectory of the second leg in both 2D and 3D Cartesian views. The final point, marked by the blue star, is achieved in 671 days and, as previously noted, is situated near the intersection of the two orbits. In order to reach the final destination, a complete revolution around the sun is performed.

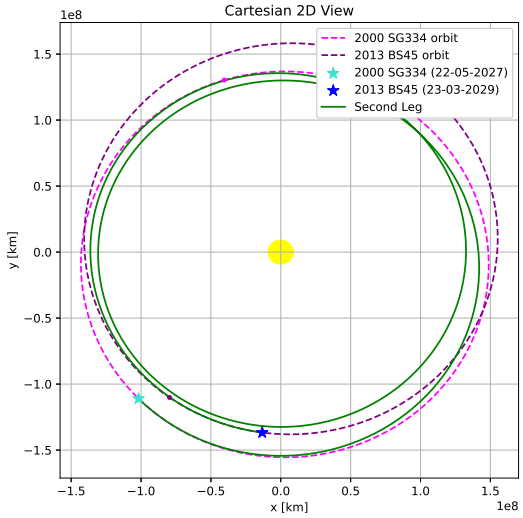

Figure 5.5: Second Leg 2D View - 671 days

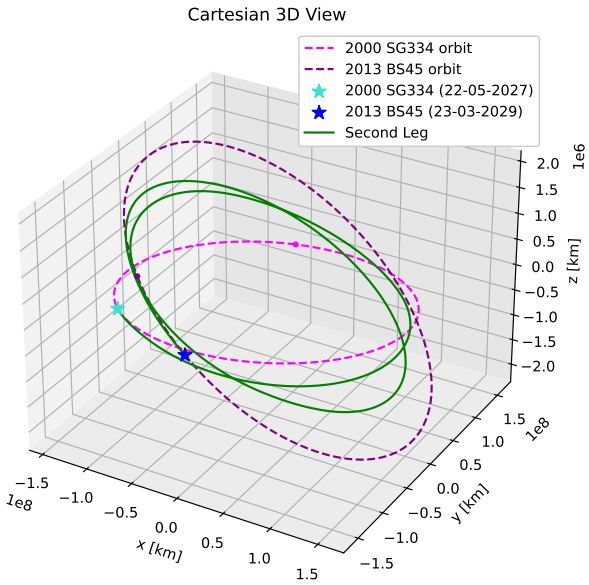

Figure 5.6: Second Leg 3D View - 671 days

Figure 5.7 illustrates a $\mathcal{S}_{\mathcal{F}}$ comprising four thrust arcs. The highest propellant consumption occurs during the second and final arcs, where significant changes in the semi-major axis, eccentricity, and inclination are executed. This maneuver's complexity demands more propellant than the previous mission segment, as evidenced by the comparison of the two total mass plots.

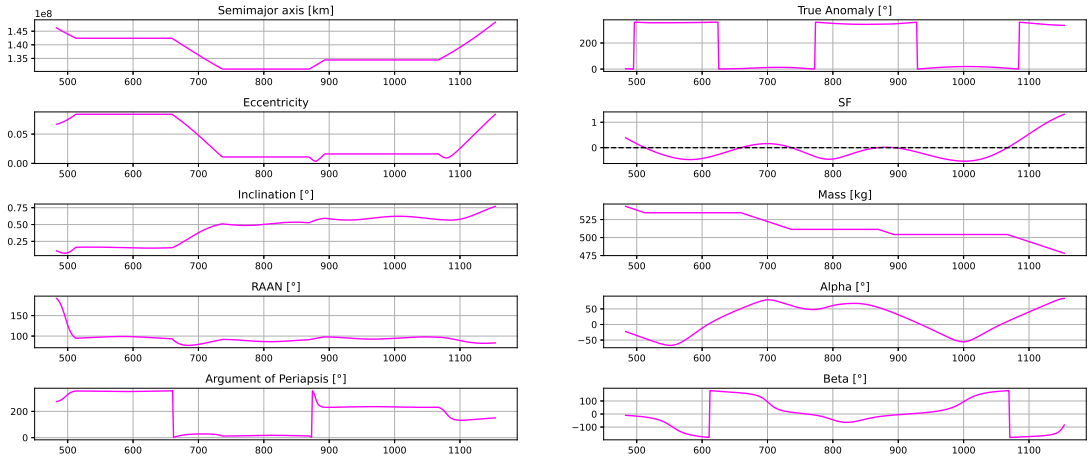

(a) a, e, i, Ω, ω **(b)** ν, $\mathcal{S}_{\mathcal{F}}$, m, α, β

Figure 5.7: Second Leg - Trends over tof [days]

Upon reaching its final destination, the mother-ship releases the second probe, marking the completion of the mission.

5.3 Complete Mission

With the mission's individual segments now defined, it is possible to present it as a whole. Table 5.3 provides a comprehensive summary of the selected departure and arrival points, delving deeper into the details as seen in Tables 3.2 and 3.3.

	Date	a [au]	e	i [°]	Ω [°]	ω [°]	ν [°]
L2	24^{th} Jan 2026	$1 + \rho_2$	0.017	0	348.74	19.06	19.0582
2000 SG344	22^{th} May 2027	0.9773	0.0668	0.11	191.76	275.51	120.2334
2013 BS45	23^{th} Mar 2029	0.9915	0.0838	0.77	83.4	150.74	30.3139

Table 5.3: Orbital parameters of the chosen asteroids

Figures 5.8 and 5.9 present the complete trajectory, with the second one highlighting both the thrust and coasting arcs.

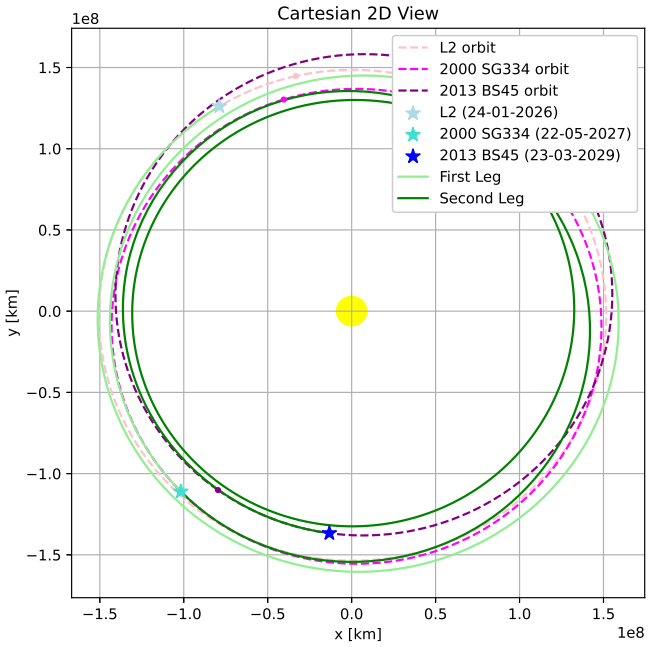

Figure 5.8: Trajectory 2D View

It is important to note that this thesis does not consider the time required for the release of each probe. In a real mission, once the desired orbit is achieved, the mother-ship would need to adjust its orientation and select the optimal moment to release the probe onto the asteroid's surface. The duration of this maneuver could vary and is therefore the subject of future studies.

Figure 5.10 reveals a noticeable discontinuity in the results, particularly in the trends of $\mathcal{S}_{\mathcal{F}}$ and m, attributed to the release of the first probe.

Finally, at the end of the mission, the spacecraft's final mass is determined to be 453 kg. With each probe weighing approximately 25 kg, this results in a total propellant consumption of 97 kg.

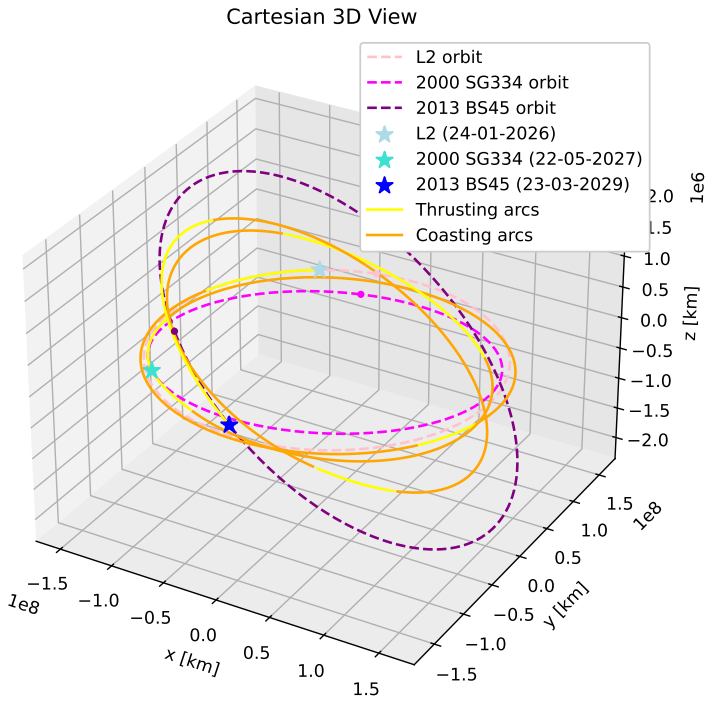

Figure 5.9: Trajectory 3D View

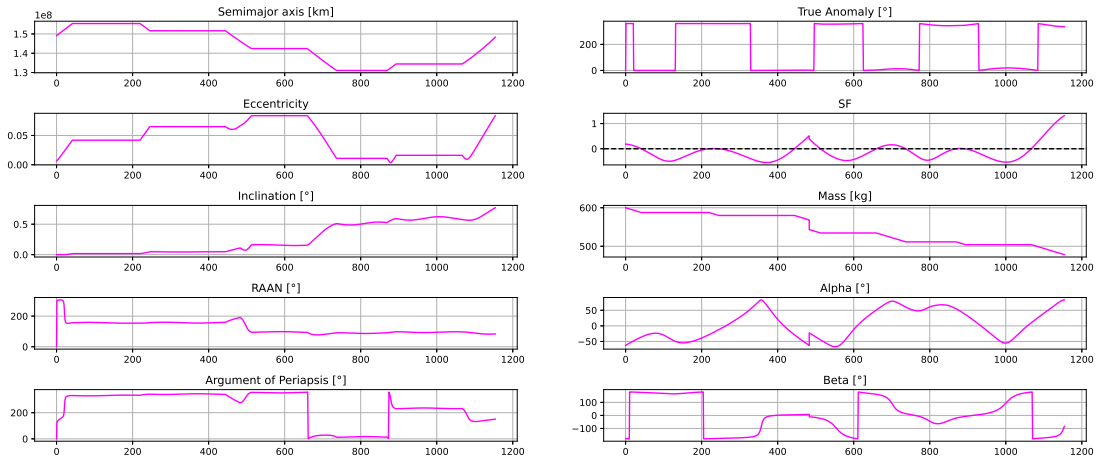

(a) a, e, i, Ω, ω **(b)** ν, $\mathcal{S}_{\mathcal{F}}$, m, α, β

Figure 5.10: Trajectory - Trends over tof [days]

Chapter 6

Conclusions

The present thesis aims to optimize low-thrust interplanetary transfers between selected asteroids. These celestial bodies harbor rare materials and essential resources, such as water, which could be invaluable for long-distance missions. The entire scenario was modeled using a heliocentric TBP.

In Chapter 4, the foundational principles of OCT were thoroughly analyzed, identifying the indirect method as an ideal approach for solving the problem. This method, while more challenging to implement, offers enhanced computational speed and code robustness. Boundary conditions were imposed on the initial and final states, leading to the implementation of a TPBVP. The combination of a single-shooting procedure and a differential corrector was crucial in accurately targeting the desired final state while updating the initial conditions. The chosen Mayer formulation, along with the PMP, facilitated the implementation of bang-bang control, alternating between thrusting and coasting arcs, and defined the optimal thrust directions.

To validate these principles and their effectiveness in solving the proposed problem, a Python code was developed and implemented. The primary goal was to minimize propellant consumption, thereby maximizing the final spacecraft's mass. This was a time-fixed problem, focusing on finding the optimal solution for the specific scenario. Achieving an absolute optimal solution will require implementing a time-variable condition in future studies.

In conclusion, this thesis successfully achieved its objective by resolving the analyzed OCP through the development of a robust and flexible tool.

6.1 Future Research

While the main objective has been successfully achieved, this work opens the door to various future improvements.

The dynamic model implementation involved a significant simplification by using the TBP and considering only gravitational effects as perturbations. For a more detailed analysis of a real-case scenario, future applications could incorporate more complex dynamic models, such as the NBP, along with other existing perturbations. Furthermore, the execution and duration of the deploying maneuver should be thoroughly analyzed.

To enhance the code's robustness and facilitate convergence, a MPBVP should be implemented instead of a TPBVP, as the trajectory involves several fly-bys, requiring additional boundary conditions at intermediate points. Consequently, each arc would have a different duration, making the problem time-variable. This approach would enable the propagation of bodies along their orbits, leading to a solution that is both locally and globally optimal. In fact, allowing the code to adjust both the start and end times would ensure convergence to the best possible solution. However, achieving convergence in such a complex scenario would be challenging. To simplify the user's experience, the code should incorporate an automatic initial guess generator.

These enhancements would transform the discussed Python code into an even more powerful tool, capable of optimizing the most complex mission scenarios.

Bibliography

[1] S. Yarlagadda. «Economics of the Stars: The Future of Asteroid Mining and the Global Economy». In: *Harward International Review* (Apr. 2022) (cit. on p. 1).

[2] NASA. *OSIRIS-REx*. URL: https://science.nasa.gov/mission/osiris-rex/ (visited on 03/20/2024) (cit. on p. 1).

[3] NASA. *Psyche*. URL: https://science.nasa.gov/mission/psyche/ (visited on 03/20/2024) (cit. on p. 1).

[4] International Astronomical Union. *Near Earth Objects*. URL: https://www.iau.org/public/themes/neo/ (visited on 03/20/2024) (cit. on p. 2).

[5] CNEOS. *Discovery Statistics*. URL: https://cneos.jpl.nasa.gov/stats/totals.html (visited on 03/20/2024) (cit. on p. 2).

[6] Shamil Biktimirov, Anne-Marlene Rüede, and Anton Ivanov. «Near-Earth Asteroids Mining as Interplanetary Economy Supply: Designing an Autonomous Mars Colony». In: Oct. 2019 (cit. on p. 2).

[7] A. A. Blagonravov. *Collected Works of K. E. Tsiolkovskiy Volume II - Reactive Flying Machines*. 1954 (cit. on p. 3).

[8] K.J. Schwenzfeger and George C. Marshall Space Flight Center. *Low Thrust Space Vehicle Trajectory Optimization Using Regularized Variables*. NASA technical report. National Aeronautics and Space Administration, 1974 (cit. on p. 4).

[9] Nathan L Parrish and Daniel J Scheeres. «Low-Thrust Trajectory Optimization with Simplified SQP Algorithm». In: *AAS/AIAA Astrodynamics Specialist Conference*. GSFC-E-DAA-TN45591-2. 2017 (cit. on p. 4).

[10] Oskar Von Stryk and Roland Bulirsch. «Direct and Indirect Methods for Trajectory Optimization». In: *Annals of Operations Research* 37 (Dec. 1992), pp. 357–373. DOI: 10.1007/BF02071065 (cit. on p. 5).

[11] I.M. Ross. *A Primer on Pontryagin's Principle in Optimal Control*. Collegiate Publishers, 2009. ISBN: 9780984357109 (cit. on p. 5).

[12] L. Mascolo. «Low-Thrust Optimal Escape Trajectories from Lagrangian Points and Quasi-Periodic Orbits in a High-Fidelity Model». PhD thesis. Politecnico di Torino, 2023 (cit. on pp. 5, 30).

[13] Stephen P. Ellner and John Guckenheimer. *Dynamic Models in Biology*. Princeton: Princeton University Press, 2006. ISBN: 9781400840960. DOI: doi:10.1515/9781400840960 (cit. on p. 6).

[14] P. Kenneth Seidelmann. *Explanatory Supplement to the Astronomical Almanac*. 1992 (cit. on p. 6).

[15] R.R. Bate, D.D. Mueller, and J.E. White. *Fundamentals of Astrodynamics*. Dover Books on Aeronautical Engineering Series. Dover Publications, 1971. ISBN: 9780486600611 (cit. on pp. 6, 20).

[16] Benjamin Stahl and Robert Braun. «Low-Thrust Trajectory Optimization Tool to Assess Options for Near-Earth Asteroid Deflection». In: *AIAA/AAS Astrodynamics Specialist Conference and Exhibit* (Aug. 2008). DOI: 10.2514/6.2008-6255 (cit. on p. 7).

[17] Ibrahim Sanad. «Design of Remote Sensing Satellite Orbit». PhD thesis. Jan. 2013. DOI: 10.13140/RG.2.2.18127.69282 (cit. on p. 11).

[18] A. Mostafa and M. Dewaik. «Balanced Low Earth Satellite Orbits». In: *Advances in Astronomy* 2020 (Aug. 2020), pp. 1–12. DOI: 10.1155/2020/7421396 (cit. on p. 11).

[19] B. Weber. *Orbital Mechanics and Astrodynamics*. 2024. URL: https://orbital-mechanics.space/classical-orbital-elements/perifocal-frame.html (visited on 05/02/2024) (cit. on p. 12).

[20] Amisha Kumari and Aayushi Deohans. *Orbital Lifetime Analysis of GTO Objects*. Oct. 2019 (cit. on p. 13).

[21] NAIF. *Ephemeris Subsystem SPK Focused on reading SPK files*. URL: https://naif.jpl.nasa.gov/pub/naif/toolkit_docs/Tutorials/pdf/individual_docs/18_spk.pdf (visited on 05/05/2024) (cit. on p. 15).

[22] Ryan S. Park, William M. Folkner, James G. Williams, and Dale H. Boggs. «The JPL Planetary and Lunar Ephemerides DE440 and DE441». In: *The Astronomical Journal* 161.3 (Feb. 2021), p. 105. DOI: 10.3847/1538-3881/abd414 (cit. on p. 15).

[23] W. Hohmann, United States. National Aeronautics, and Space Administration. *The Attainability of Heavenly Bodies*. NASA technical translation. National Aeronautics and Space Administration, 1960 (cit. on p. 18).

[24] MathWorks. *Hohmann Transfer with the Spacecraft Dynamics Block*. URL: https://it.mathworks.com/help/aeroblks/hohmann-transfer-with-the-spacecraft-dynamics-block.html (visited on 05/06/2024) (cit. on p. 19).

[25] ESA. *What is a Launch Window?* URL: https://www.esa.int/Science_Exploration/Space_Science/What_is_a_launch_window (visited on 05/08/2024) (cit. on p. 20).

[26] B. Weber. *Interplanetary Trajectories*. 2024. URL: https://orbital-mechanics.space/interplanetary-maneuvers/interplanetary-transfer-phasing.html (visited on 05/08/2024) (cit. on pp. 21, 24, 25, 27–29).

[27] Neil J. Cornish. *The Lagrange Points*. 1998. URL: https://web.archive.org/web/20150907090116/http://www.physics.montana.edu/faculty/cornish/lagrange.pdf (visited on 09/08/2024) (cit. on p. 29).

[28] ESA. «Asteroids Numbers and Names». In: *ESA science and technology* (Sept. 2019) (cit. on p. 34).

[29] University of Arizona. «How many asteroids are there?» In: (2024) (cit. on p. 34).

[30] JPL. *Horizon System*. URL: https://ssd.jpl.nasa.gov/horizons/app.html#/ (visited on 09/27/2024) (cit. on p. 34).

[31] Kris Zacny, Phil Chu, Jack Craft, Marc Cohen, Warren James, and Brent Hilscher. «Asteroid Mining». In: Sept. 2013. DOI: 10.2514/6.2013-5304 (cit. on p. 36).

[32] Alexander Braun, Martin Connors, Robert E. Zee, Yaoguo Li, Kieran Carroll, Henry Spencer, and Daniel Britt. «The Geophysical Reconnaissance Asteroid Surface Probe (GRASP), a lander mission to determine asteroid density distribution». In: *42nd COSPAR Scientific Assembly*. Vol. 42. July 2018, B0.2-20-18, B0.2-20–18 (cit. on p. 36).

[33] J. Stoer and R. Bulirsch. *Introduction to Numerical Analysis*. NY: Springer New York, 1980 (cit. on p. 39).

[34] Linda Petzold. «Automatic Selection of Methods for Solving Stiff and Nonstiff Systems of Ordinary Differential Equations». In: *SIAM Journal on Scientific and Statistical Computing* 4 (Mar. 1983). DOI: 10.1137/0904010 (cit. on p. 41).

[35] R. Courant and D. Hilbert. *Methods of Mathematical Physics, Volume 1*. v. 1. Wiley, 2008. ISBN: 9783527617227 (cit. on p. 42).

[36] L. Pallottino. «Sistemi Robotici Distribuiti». In: 2012. Chap. 5 (cit. on p. 42).

[37] I.M. Gelfand, S.V. Fomin, and R.A. Silverman. *Calculus of Variations*. Dover Books on Mathematics. Dover Publications, 2000. ISBN: 9780486414485 (cit. on p. 42).

[38] R.E. Bradley and E. Sandifer. *Leonhard Euler: Life, Work and Legacy*. ISSN. Elsevier Science, 2007. ISBN: 9780080471297 (cit. on p. 42).

[39] Herman H. Goldstine. *A History of the Calculus of Variation from the 17th century through the 19th century*. Studies in the History of Mathematics and Physical Sciences. Springer New York, NY, 2012. ISBN: 9781461381068 (cit. on p. 42).

[40] A.E. Bryson. «Optimal control-1950 to 1985». In: *IEEE Control Systems Magazine* 16.3 (1996), pp. 26–33. DOI: 10.1109/37.506395 (cit. on p. 42).

[41] L.F. Shampine and M.K. Gordon. *Computer Solution of Ordinary Differential Equations: The Initial Value Problem*. W. H. Freeman, 1975. ISBN: 9780716704614 (cit. on p. 50).

[42] F.R. Moulton. *New Methods in Exterior Ballistics*. Goldstine Printed Materials. University of Chicago Press, 1926 (cit. on p. 50).

[43] D.F. Lawden. *Optimal Trajectories for Space Navigation*. Butterworths mathematical texts. Butterworths, 1963 (cit. on p. 52).